Permutational symmetry, isotope effects, side crossing, and singlet-triplet splitting in anthracene·He_N ($N=1, 2$) clusters

Andreas Heidenreich and Joshua Jortner
School of Chemistry, Tel Aviv University, 69978 Tel Aviv, Israel

(Received 10 December 2002; accepted 24 February 2003)

We present quantum-mechanical calculations for the vibrational states of anthracene·^3He_N and anthracene·^4He_N ($N=1, 2$) clusters in the ground (S_0) and first excited singlet state (S_1) of the anthracene molecule. The anthracene-He potential in the S_0 state was described in terms of a sum of Lennard-Jones atom-atom potentials, while the potential in the S_1 state also included changes in the dispersive energy and in the repulsive interactions. Variational calculations were carried out for anthracene·He_1. For anthracene·He_2, configuration interaction calculations were performed, accounting for the boson and fermion permutation symmetry. For both helium isotopes of the $N=1$ cluster, tunneling splitting is negligible (<0.01 cm^{-1}), as an appreciable interaction of the densities was only found for highly excited states above the potential-energy barrier of side crossing (for energy eigenvalues $\geqslant -22$ cm^{-1} below the dissociation limit). The two-boson anthracene·$^4He_2$ system assumes a singlet $^1A_1$ ground state due to zero spin of the ^{4}He isotope. Because of the dominance of the two-particle over the one-particle interactions, the two-fermion anthracene·$^3He_2$ system has a triplet ($^3B_2$) vibrational ground state. The singlet-triplet (1^3B_2-1^1B_2) splitting between the two lowest states of the same spatial symmetry of anthracene·$^3He_2$ was calculated to be 10.5 cm^{-1}. Mass and permutation symmetry effects on the vibrational level structure of anthracene·He_1 and anthracene·He_2 were explored for anthracene·$^4He_1$, anthracene·$^3He_1$, the two-boson system anthracene·$^4He_2$, the two-fermion system anthracene·$^3He_2$ and for the hypothetical fermion system of mass 4. While the isotope effect on the zero-point energies ε_0 in the S_0 state is $\Delta\varepsilon_0^{(1)}/\varepsilon_0^{(1)}=[\varepsilon_0(\text{anthracene}\cdot{}^3\text{He}_1)-\varepsilon_0(\text{anthracene}\cdot{}^4\text{He}_1)]/\varepsilon_0(\text{anthracene}\cdot{}^4\text{He}_1)=12\%$, in accord with the mass effect in the harmonic approximation, the zero-point energy difference between the ground states of the two-fermion anthracene·$^3He_2$ and the two-boson anthracene·$^4He_2$ system is $\Delta\varepsilon_0^{(2)}/\varepsilon_0^{(2)}=[\varepsilon_0(\text{anthracene}\cdot{}^3\text{He}_2)-\varepsilon_0(\text{anthracene}\cdot{}^4\text{He}_2)]/\varepsilon_0(\text{anthracene}\cdot{}^4\text{He}_2)=10\%$, manifesting a cancellation of mass and permutation symmetry effects. The isotope effect on the red spectral shift δ of the electronic origin for the $S_0\rightarrow S_1$ transition of anthracene·He_1 is $\Delta\delta^{(1)}=\delta(\text{anthracene}\cdot{}^4\text{He}_1)-\delta(\text{anthracene}\cdot{}^3\text{He}_1)=0.28$ cm^{-1}, while $\Delta\delta^{(2)}=\delta(\text{anthracene}\cdot{}^4\text{He}_2)-\delta(\text{anthracene}\cdot{}^3\text{He}_2)=-0.50$ cm^{-1}, being of the opposite sign than $\Delta\delta^{(1)}$. These features of the spectral shifts as well as the small isotope effects on the energetics and Franck-Condon factors for the $S_0\rightarrow S_1$ vibronic spectra exhibit a delicate balance between differences in mass effects, He-He repulsion, and permutational symmetry of the boson and fermion systems. © *2003 American Institute of Physics.* [DOI: 10.1063/1.1567715]

I. INTRODUCTION

The exploration of the energy landscapes, spatial structures and shapes, energetics, electronic-nuclear level structure, spectroscopy, dynamics, and chemical reactivity of clusters[1–3] provides the conceptual and practical basis for the elucidation of the optical, electrical, magnetic, chemical, and biophysical response of nanostructures.[4,5] A significant development in this broad and interdisciplinary research area of cluster chemical physics pertains to the fascinating properties of quantum clusters, where the spatial configuration, nuclear level structure, and dynamics is dominated by quantum effects and by permutational symmetry.[6–19] Notable examples involve ^4He_N ($N\geqslant 2$) and ^3He_N ($N\geqslant 25$) quantum clusters, which exhibit large zero-point energy motion, being the only clusters which are liquids and devoid of a rigid structure close to 0 K. These quantum clusters manifest boson (for ^{4}He) (Refs. 18–23) and fermion (for ^{3}He) (Refs. 24 and 25) permutation symmetry. The most important properties of a sufficiently large, finite boson ^4He_N cluster (e.g., $N\approx 64$) (Ref. 18) are superfluidity and Bose–Einstein condensation, both of which manifest the implications of permutational symmetry.[18–23] Finite ^4He_N systems reveal the occurrence of a rounded-off lambda transition,[18] the microscopic analog of the hydrodynamic effects of the response of a superfluid to the motion to its boundaries[23,26–29] and the coupling of elementary roton-type collective excitation to a molecular impurity.[21] A finite sufficiently large fermion ^3He_N cluster is expected to reveal the features of a confined Fermi liquid and onset of superfluidity (superconductivity) in the mK temperature range, in analogy to the ^{3}He bulk system,[30] but the characteristics of these finite systems were not yet subjected to experimental or theoretical scrutiny. In analogy to the bulk ^{3}He, one expects that in the temperature domain >10 mK the ^3He_N clusters constitute a finite Fermi liquid.

A variety of molecules have been spectroscopically studied in large ^4He_N clusters at 0.4 K, acting as microscopic probes for superfluidity. These involve smaller species, e.g., OCS,[23,26] SF_6,[27] and linear monomers[28,29] studied by rotational-vibrational spectroscopy, glyoxal[21] and aromatic molecules, e.g., anthracene and tetracene,[31] studied by electronic spectroscopy, which provided information on superfluid friction effects, coupling with elementary excitations and local solvation in the superfluid. In contrast, ^3He_N large clusters formed at 0.15 K do not exhibit superfluidity and the spectroscopic features of probe molecules in these clusters correspond to solvation in a ''normal'' Fermi cluster.[24,25] The studies of molecular probes for superfluidity in ^4He_N boson clusters or the lack of it in ^3He_N fermion clusters raise a renewed interest in small aromatic molecule$\cdot He_N$ clusters,[31–47] which are expected to exhibit interesting features of nuclear quantum effects and permutational symmetry effects. On the theoretical front, accurate quantum-mechanical studies of 2,3-dimethyl naphthalene$\cdot^4$He complex were conducted by Bach, Leutwyler, Szabo, and Bacic,[44] variational calculations for anthracene$\cdot^4$He and configuration interaction calculations were performed by Heidenreich, Even, and Jortner,[47] and quantum path-integral Monte Carlo simulations for benzene$\cdot^4He_{30}$ were reported by Kwon and Whaley.[48] Relevant studies for aromatic molecule$\cdot^3He_N$ clusters involve the quantum-mechanical calculations for the $SF_6\cdot^3He_N$ ($N=1,2$) fermion clusters reported by Jungwirth and Krylov.[49] In this paper, we present quantum-mechanical calculations for the energetics, nuclear dynamics, and electronic-vibrational spectroscopy of An $\cdot^4He_N$ and An$\cdot^3He_N$ (An=anthracene,$N=1,2$) clusters in the ground (S_0) and in the first spin-allowed excited (S_1) electronic states. From the technical point of view, the variational studies for An$\cdot^4He_1$ and An$\cdot^3He_1$ utilize a considerably larger basis than previously used for An$\cdot^4He_1$.[47] From the point of view of methodology, we extended our previous methods for configuration interaction in the An$\cdot^4He_N$ boson systems[47] to the corresponding An$\cdot^3He_N$ fermion systems. We explored isotope effects and the implications of permutation symmetry on the nuclear level structure, in particular the singlet-triplet splitting in the An$\cdot^3He_2$ fermion cluster. In the context of nuclear level structure, the issue of tunneling splitting and side crossing in the An$\cdot^4He_1$ and An$\cdot^3He_1$ clusters is of interest. In the context of electronic-vibrational level structure, novel information was obtained on spectral shifts and Franck-Condon factors for the $S_0\rightarrow S_1$ transition in the An$\cdot^4He_N$ and An$\cdot^3He_N$ ($N=1,2$) quantum clusters.

II. METHODOLOGY

A. Potentials

Since part of the methodology was already described in our previous paper,[47] it will be only briefly outlined here. In all our calculations we treated the anthracene molecule as a rigid and spatially fixed structure, disregarding the intramolecular vibrations of anthracene and the vibrational-rotational coupling. In the ground electronic state S_0 of anthracene, the anthracene-He potential V_0 was described in terms of a sum of atom-atom Lennard-Jones 6-12 potentials. We have utilized the potential parameters $\sigma_{C-He}=3.099$ Å, $\varepsilon_{C-He}=13.92\ cm^{-1}$, $\sigma_{H-He}=2.903$ Å, and $\varepsilon_{H-He}=5.761\ cm^{-1}$, which were taken from Lim.[50] For the S_1 state of anthracene, the anthracene-helium potential V_1 was obtained by modifying the ground-state potential V_0 by two additional terms:

$$V_1=V_0+V_{DSS}+\Delta V_{LJ}, \tag{1}$$

where V_{DSS} and ΔV_{LJ} are the changes in the dispersive and repulsive energies, respectively, of the S_1 and the S_0 electronic states. V_{DSS} causes a stabilization of the excited-state potential, which leads to a red spectral shift of the 0-0 vibronic transition. V_{DSS} was obtained by the dispersive spectral shift (DSS) theory of Shalev and Jortner,[51] calculating the dispersive difference potential in a semiempirical perturbative configuration interaction calculation from the Hückel molecular orbitals of the aromatic molecule and the polarizability and ionization energy of the rare-gas atoms. The term ΔV_{LJ} represents the difference of the Lennard-Jones repulsive term of the S_1 and S_0 states,

$$\Delta V_{LJ}=4\varepsilon\,\frac{\sigma_{ex}^{12}-\sigma^{12}}{R^{12}}, \tag{2}$$

with the excited state parameter σ_{ex}. σ_{ex} together with the adjustable dimensionless parameter η of the DSS theory[51] was chosen such that the experimental spectral shifts[46] of $-1.6\ cm^{-1}$ of the $(1|0)$ structure and $-11.0\ cm^{-1}$ of the $(2|0)$ structure were reproduced by the quantum-mechanical calculations.[47] The values are $\eta=0.60$ and $\sigma_{ex}=1.0285\sigma$, where the repulsive difference potential was applied only to the carbon atoms in 9,10 position. Figure 1 shows contour plots of the S_0 and the S_1 state potentials for anthracene $\cdot He_1$. The potential-energy surfaces are differently shaped but both have almost identical well depths of $-138.10\ cm^{-1}$ for the S_0 and $-138.06\ cm^{-1}$ for the S_1 state.

For the He-He potential we used the *ab initio* potentials of Vos, van Lenthe, and Duijnenveldt[52] and of Ceperley and Partridge,[53] tabulated and reviewed by Aziz and Slaman.[54] For convenience and for a future analytical calculation of the two-particle integrals we fitted this potential to a linear combination of three Gaussians centered at the He–He distance $R=0$,

$$V(R)=\sum_{i=1}^{3} g_i \exp(-R^2/2\gamma_i^2). \tag{3}$$

The fitted expansion coefficients g_i and Gaussian exponents γ_i are tabulated in our previous paper.[47]

B. Basis sets and variational calculations for anthracene$\cdot He_1$

We have performed variational calculations for anthracene$\cdot He_1$ (Ar$\cdot He_1$), using the following ansatz for the wave function $\psi(x,y,z)$ of the helium atom in the potential well of the rigid aromatic molecule structure:

$$\Psi(x,y,z)=\sum_{\mu=1}^{n} c_\mu \phi_\mu(x,y,z), \tag{4}$$

where c_μ denotes the expansion coefficients, x and y denote the short and the long molecular axis, respectively, with the

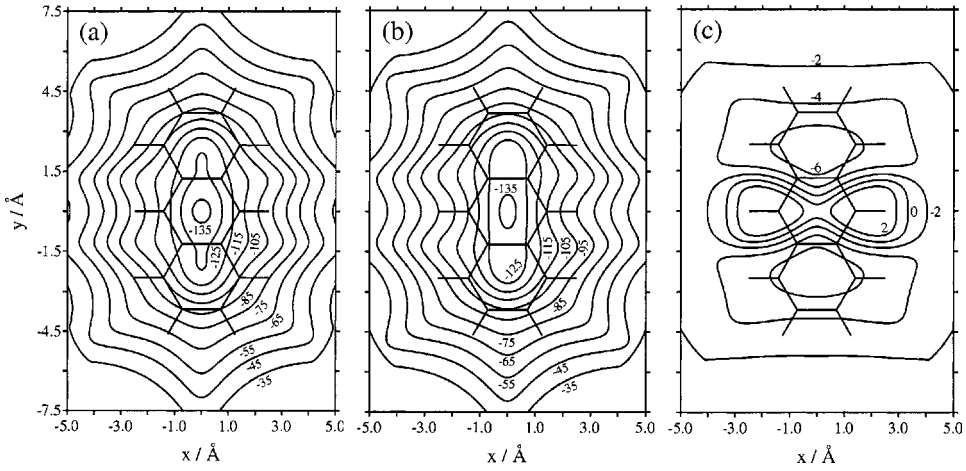

FIG. 1. The contour maps of the anthracene-helium potential energy hypersurfaces, (a) the S_0, (b) the S_1 state potential, and (c) the difference potential. For each point in the *xy* plane, the *z* coordinate was optimized according to the minimum potential energy at that point. For the difference potential, the *z* coordinate was optimized for the S_0 state potential.

center of mass of the anthracene molecule as the origin of the coordinate system. The three-dimensional (3D) basis functions $\phi_\mu(x,y,z)$ were taken as products of one-dimensional (1D) functions,

$$\phi_\mu(x,y,z)=\phi_{\mu x}(x)\phi_{\mu y}(y)\phi_{\mu z}(z). \tag{5}$$

The 1D functions $\phi_{\mu x}(x)$, $\phi_{\mu y}(y)$; and $\phi_{\mu z}(z)$ are the numerical solutions of the Schrödinger equation for one-dimensional cuts $V_{y=0,z=\mathrm{opt}}(x)$, $V_{x=0,z=\mathrm{opt}}(y)$, and $V_{x=0,y=0}(z)$ of the intermolecular anthracene-helium potential $V_0(x,y,z)$. Specifically, the cuts $V(x)$ and $V(y)$ were obtained for fixed values $y=0$ and $x=0$, respectively, and the *z* coordinate was optimized with respect to the minimum energy for the given *x*,*y* coordinates, while $V(z)$ was taken at $x=0$ and $y=0$. Figure 2 shows the numerical solutions of the 1D Schrödinger equation up to the 1D quantum numbers $\mu_x=8$, $\mu_y=18$, and $\mu_z=3$ for the ^{4}He isotope.

Each 3D product function $\phi_\mu(x,y,z)$ is completely characterized by the triplet (μ_x,μ_y,μ_z) of 1D quantum numbers. Since the 1D functions are orthonormal and symmetry adapted, so are the 3D product functions. The symmetry of the 3D functions is determined by the framework of the rigid molecular structure, which is C_{2v}, if only one side of the aromatic molecule is considered, and D_{2h}, if both sides are involved. As depicted in Fig. 2(c), *z* is restricted to positive *z* values, i.e., the functions $\phi_{\mu z}(z)$ span only the space on one side of the aromatic molecule. Consequently, the constructed 3D functions correspond to the point group C_{2v}. Basis functions for the point group D_{2h} are obtained by symmetric and antisymmetric linear combinations of the functions $\phi_{\mu z}(z)$ with respect to the molecular *xy* plane.

We have employed three 3D basis sets. All of them are based on the 1D functions for ^{4}He. These basis sets have been utilized for all variational calculations of An·^{4}He$_1$, An·^{3}He$_1$, An·^{4}He$_2$, and An·^{3}He$_2$ presented in this paper. Our small basis set, denoted as basis set A, comprises all 1D functions up to $\mu_x=4$, $\mu_y=10$, and $\mu_z=2$, and is restricted only to one side of the molecule, so that the resulting 3D basis functions are symmetry adapted with respect to the point group C_{2v}. This basis set consists of 165 basis functions, among them 54 A_1 symmetry-adapted functions, and was employed throughout in our previous paper.[47] As a consequence of the restriction of the basis set to one side of the molecule, tunneling splitting and side crossing cannot be described by this basis set.

An intermediate basis set *B* spans both sides of the aromatic molecule and is therefore symmetry adapted with respect to point group D_{2h}. It contains all possible 1368 3D functions (among them 200 of A_g symmetry), which arise

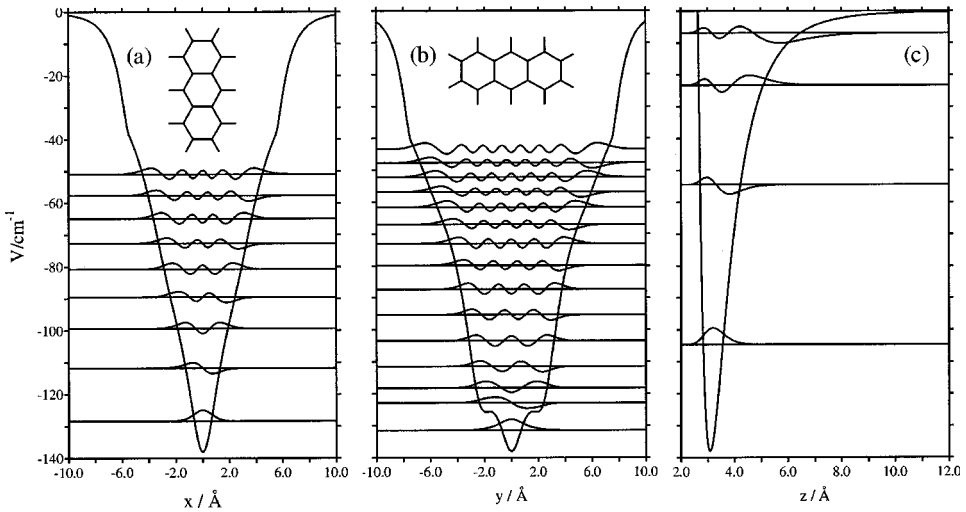

FIG. 2. One-dimensional cuts of the anthracene-helium ground electronic state potential along the *x*, *y*, and *z* axes. For cut (a) along the *x* axis, *y* was set to 0 and the *z* axis was optimized according to the minimum potential energy for the given *x*, *y* pair. Cut (b) along the *y* axis was taken at $x=0$ with the *z* axis being optimized. Cut (c) was taken at $x=0$, $y=0$. The numerically obtained 1D eigenfunctions, which served as basis functions in the subsequent variational calculations, are included in the diagrams up to 1D quantum numbers $\mu_x=8$, $\mu_y=18$, and $\mu_z=3$. To compare their spatial extension with the size of the molecule, the anthracene molecule has been included at the same scale.

from the 1D functions up to $\mu_x=8$, $\mu_y=18$, and all symmetric and antisymmetric linear combinations of functions $\phi_{\mu z}(z)$ up to $\mu_z=3$.

The large basis set C contains all basis functions of set B and is augmented by additional symmetry-adapted pairs of Gaussian functions centered at large x and y values, i.e., at the molecular periphery beyond the functions $\mu_x=8$, $\mu_y=18$, as well as by Gaussians close to the molecular xy plane. The Gaussians have an exponent of $\sigma=0.4$ Å and are located at $x=\pm 4.8$, ± 5.4, ± 6.0, and ± 6.6 Å, at $y=\pm 9.0$, ± 9.6, ± 10.2, ± 10.8, and ± 11.4 Å, and at $z=\pm 0.3$, ± 0.9, ± 1.5, and ± 2.1 Å. The total number of 3D functions is 7888, 1080 of them are of A_g symmetry. Basis set C is not orthonormal, so that the Hamiltonian matrix has been Löwdin orthogonalized.

C. Variational calculations of anthracene·He_2

The Hamiltonian of the An·He_2 system is

$$\hat{H}=\hat{h}(1)+\hat{h}(2)+\hat{g}(1,2), \tag{6}$$

where $\hat{h}(1)$ and $\hat{h}(2)$ are the one-particle operators, consisting of the kinetic energy operators of the helium atoms and the potential-energy operator of the helium in the field of the aromatic molecule. $\hat{g}(1,2)$ is the two-particle potential-energy operator of the two helium atoms. In the approximation of a rigid aromatic molecule structure, the Hamiltonian has analogies to that of a two-electron atom: the aromatic molecule has the role of the atomic core and the helium atoms correspond to the electrons. We have performed configuration interaction (CI) calculations for An·$^4He_2$ and An·$^3He_2$. The nuclear wave functions were taken as linear combinations of Hartree products, which are symmetrized for the two-boson An·$^4He_2$ system and antisymmetrized for the two-fermion An·$^3He_2$ system,

$$\Psi(1,2)=\sum_a (c_a\Delta_a(1,2)), \tag{7}$$

with 1 and 2 denoting the Cartesian coordinates of the two bosons and the Cartesian and spin coordinates of the two fermions. The configurations are built up by the 3D orthonormal basis functions ϕ_μ defined in Sec. II B and are spin and symmetry adapted. For the two-boson An·$^4He_2$ system of spin 0, there are two types of singlet configurations, denoted as type 1, $^1\Delta_1(\mu,\mu)$, and type 2, $^1\Delta_2(\mu,\nu)$, respectively, in which the two bosons occupy the same orbitals ϕ_μ or different orbitals ϕ_μ and ϕ_ν,

$$^1\Delta_1(\mu,\mu)=\phi_\mu(1)\phi_\mu(2), \tag{8}$$

$$^1\Delta_2(\mu,\nu)=\frac{1}{\sqrt{2}}[\phi_\mu(1)\phi_\nu(2)+\phi_\nu(1)\phi_\mu(2)]. \tag{9}$$

Since the spin of the ^{4}He atoms is 0, the configurations do not contain spin functions.

In the case of the two-fermion system An·$^3He_2$, each ^{3}He atom has spin $\frac{1}{2}$, so that the system assumes either a singlet or a triplet state. The arsenal of electronic structure theory is now directly applicable to the two-fermion system. The configurations $\Delta_a(1,2)$ in the CI expansion, Eq. (7), are then spin-adapted linear combinations of Slater determinants. There are two types of singlet configurations, $^1\Delta_1(\mu,\mu)$ and $^1\Delta_2(\mu,\nu)$:

$$^1\Delta_1(\mu,\mu)=\frac{1}{\sqrt{2}}[\phi_\mu(1)\alpha(1)\phi_\mu(2)\beta(2) - \phi_\mu(2)\beta(2)\phi_\mu(1)\alpha(1)], \tag{10}$$

$$^1\Delta_2(\mu,\nu)=\tfrac{1}{2}[\phi_\mu(1)\alpha(1)\phi_\nu(2)\beta(2) - \phi_\mu(2)\alpha(2)\phi_\nu(1)\beta(1) - \phi_\mu(1)\beta(1)\phi_\nu(2)\alpha(2) + \phi_\mu(2)\beta(2)\phi_\nu(1)\alpha(1)]. \tag{11}$$

The matrix elements of the singlet configurations of the two-fermion system are identical to those of the two-boson system:

$$\langle ^1\Delta_1(\mu,\mu)|^1\Delta_1'(\nu,\nu)\rangle=2h_{\mu\nu}\delta_{\mu\nu}+(\mu\nu|\mu\nu), \tag{12}$$

$$\langle ^1\Delta_1(\mu,\mu)|^1\Delta_2(\lambda,\sigma)\rangle=\sqrt{2}[h_{\mu\lambda}\delta_{\mu\sigma}+h_{\mu\sigma}\delta_{\mu\lambda}+(\mu\lambda|\mu\sigma)], \tag{13}$$

$$\langle ^1\Delta_2(\mu,\nu)|^1\Delta_2'(\lambda,\sigma)\rangle=h_{\mu\lambda}\delta_{\nu\sigma}+h_{\mu\sigma}\delta_{\nu\lambda}+h_{\nu\sigma}\delta_{\mu\lambda} + h_{\nu\lambda}\delta_{\mu\sigma}+(\mu\lambda|\nu\sigma)+(\mu\sigma|\nu\lambda) \tag{14}$$

with

$$h_{\mu\nu}=\int d\tau_1\phi_\mu(1)\hat{h}(1)\phi_\nu(1) \tag{15}$$

and

$$(\mu\nu|\lambda\sigma)=\int d\tau_1\int d\tau_2\phi_\mu(1)\phi_\nu(1)\hat{g}(1,2)\phi_\lambda(2)\phi_\sigma(2), \tag{16}$$

where τ_1 and τ_2 denote the entire three-dimensional definition range of helium atoms 1 and 2, respectively. The triplet configurations were chosen for a magnetic quantum number $M_S=0$:

$$^3\Delta_2(\mu,\nu)=\tfrac{1}{2}[\phi_\mu(1)\alpha(1)\phi_\nu(2)\beta(2) - \phi_\mu(2)\alpha(2)\phi_\nu(1)\beta(1) + \phi_\mu(1)\beta(1)\phi_\nu(2)\alpha(2) - \phi_\mu(2)\beta(2)\phi_\nu(1)\alpha(1)]. \tag{17}$$

The matrix elements are:

$$\langle ^3\Delta_2(\mu,\nu)|^3\Delta_2'(\lambda,\sigma)\rangle=h_{\mu\lambda}\delta_{\nu\sigma}-h_{\mu\sigma}\delta_{\nu\lambda}+h_{\nu\sigma}\delta_{\mu\lambda} - h_{\nu\lambda}\delta_{\mu\sigma}+(\mu\lambda|\nu\sigma)-(\mu\sigma|\nu\lambda). \tag{18}$$

Using the small basis set A for point group C_{2v}, we have performed full CI calculations, generating all possible configurations. This resulted in 3600 configurations and 2.3×10^7 He–He integrals for each symmetry type. All one- and two-particle integrals were solved numerically, as described in our previous paper.[47]

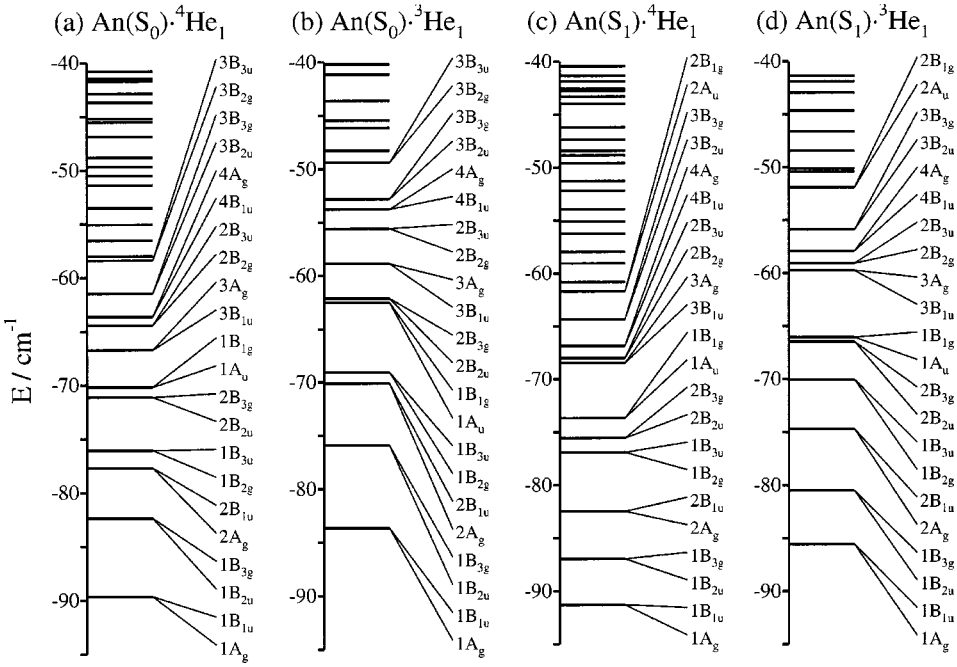

FIG. 3. The vibrational level diagrams for the An·^{4}He$_1$ and An·^{3}He$_1$ complexes in the S_0 and the S_1 electronic states of the anthracene molecule.

III. RESULTS AND DISCUSSION

A. Anthracene·He$_1$

Figure 3 shows the vibrational eigenvalue spectra of the An·He$_1$ complexes for ^{4}He and ^{3}He in the S_0 and the S_1 state of anthracene in the energy range up to -40 cm^{-1} below the dissociation limit. The energies of the lowest eigenstates of each symmetry type are summarized in Table I. The calculations rest on the extended basis set C, i.e., $\approx$1000 basis functions per symmetry type and correspond to the D_{2h} two-sided molecular framework.

In all the four eigenvalue spectra portrayed in Fig. 3, a pair of quasidegenerate A_g and B_{1u} states constitute the lowest vibrational states of the system. These A_g and B_{1u} states are symmetric or antisymmetric with respect to the molecular plane, respectively, but otherwise identical. The tunneling splitting for these states is very small and is masked by the error (0.01 cm^{-1}) of the numerical evaluation of the one-particle integrals. The zero-point energies ε_0 are 48.5 (^{4}He) and 54.5 cm^{-1} (^{3}He) for the S_0 state and 46.8 (^{4}He) and 52.5 cm^{-1} (^{3}He) for the S_1 state potential. The isotope effect $\Delta\varepsilon_0/\varepsilon_0$(An·^{4}He$_1$)$\approx$12% is in accord with the harmonic approximation (15%). The ground-state wave functions consist almost exclusively of the basis function ϕ_{000}; the linear-expansion coefficients are 0.99 (^{4}He) and 0.97 (^{3}He) for the S_0 state potential, and 0.95 (^{4}He) and 0.93 (^{3}He) for the S_1 state potential of the anthracene-helium system. Also the lower excited states are described mainly by a single 3D basis function, whose linear-expansion coefficients still assume values around 0.9.

An appreciable energy splitting, which originates from the interaction of the probability densities on both sides of the aromatic molecule, emerges only for states above ≈-22 cm^{-1}. Below ≈-22 cm^{-1}, all states, which are distinguished by the nodal behavior with respect to the molecular (xy) plane, are quasidegenerate (energy splitting $\leqslant$0.01 cm^{-1}), so that a single-sided treatment of the system within the framework of point group C_{2v} is possible without loss of accuracy. Above ≈-22 cm^{-1}, the states in the C_{2v} framework of the two independent molecular surfaces split as follows: A_1:A_g+B_{1u}, B_2:$B_{2u}+B_{3g}$, A_2:$B_{1g}+A_u$, and B_1:$B_{3u}+B_{2g}$.

In our previous paper[47] we already addressed the calculation of vibronic spectra, but only for ^{4}He and the much smaller basis set A. We now address isotope effects on the $S_0\rightarrow S_1$ vibronic spectra using the extended basis set C. The lowest excited vibrational states of the An·^{4}He$_1$ and of the An·^{3}He$_1$ complexes are the two quasidegenerate $1B_{2u}$ and $1B_{3g}$ states (Table I). Both states are 7.34 cm^{-1} (^{4}He) and 7.73 cm^{-1} (^{3}He) above the $1A_g$ and $1B_{1u}$ ground states. This means that under the experimental conditions[46] of 0.4 K, only the ground vibrational states $1A_g$ and $1B_{1u}$ are thermally populated and can act as initial S_0 vibronic states for the $S_0\rightarrow S_1$ excitation. The selection rules of the $S_0\rightarrow S_1$ transition allow then for two series of vibronic transitions, which are the $1A_g\rightarrow nA_g$ and the $1B_{1u}\rightarrow nB_{1u}$ series. Figure 4 exhibits the transition frequencies and the Franck-Condon factors for An·^{4}He$_1$ and An·^{3}He$_1$ in terms of stick spectra in the range up to 60 cm^{-1} above the 0–0 transition. This energy interval covers the experimentally observed range[46] and contains all transitions of appreciable intensity. Since tunneling splitting is negligible ($<$0.01 cm^{-1}) in this energy range, the $1A_g\rightarrow nA_g$ and the $1B_{1u}\rightarrow nB_{1u}$ series are quasidegenerate. The most prominent transitions are classified by [x], [y], and [z], respectively, according to the dominant contribution of the 3D basis functions $\phi_{\mu x,0,0}$, $\phi_{0,\mu y,0}$, $\phi_{0,0,\mu z}$ to the excited-state wave function. There are also ''mixed'' transitions such as [xy], in which the excited-state wave function consists mainly of basis functions $\phi_{\mu x,\mu y,0}$, but transitions to these states have only little intensity. The spectral shift δ of the 0-0 vibronic band with respect to the position of the bare anthracene molecule is given by the energy ei-

TABLE I. The energies of the lowest vibrational state for each symmetry for the $An\cdot He_1$ and $An\cdot He_2$ [for $An\cdot{}^3He_2$, $An\cdot{}^4He_2$, and $An\cdot{}^4He_2$(hyp.)], as well as the minima of the anthracene-helium potentials.

		S_0 state potential E/cm^{-1}	S_1 state potential E/cm^{-1}
$An\cdot{}^4He_1$	$A_1(A_g+B_{1u})$	−89.64	−91.27
	$B_2(B_{2u}+B_{3g})$	−82.37	−86.95
	$A_2(B_{1g}+A_u)$	−70.17	−73.67
	$B_1(B_{3u}+B_{2g})$	−76.09	−76.90
$An\cdot{}^3He_1$	$A_1(A_g+B_{1u})$	−83.65	−85.55
	$B_2(B_{2u}+B_{3g})$	−75.92	−80.51
	$A_2(B_{1g}+A_u)$	−62.52	−66.04
	$B_1(B_{3u}+B_{2g})$	−69.06	−70.02
Minimum potential energy		−138.10	−138.06

		S_0 state potential		S_1 state potential	
		Singlet E/cm^{-1}	Triplet[a] E/cm^{-1}	Singlet E/cm^{-1}	Triplet[a] E/cm^{-1}
$An\cdot{}^4He_2$	A_1	−159.28	−154.87	−169.94	−163.55
	B_2	−150.89	−160.78	−159.30	−171.39
	A_2	−149.28	−147.72	−158.38	−157.34
	B_1	−147.42	−149.53	−157.18	−158.52
$An\cdot{}^3He_2$	A_1	−147.04	−141.48	−157.26	−149.64
	B_2	−137.80	−148.52	−145.65	−158.68
	A_2	−136.37	−134.34	−144.93	−143.55
	B_1	−134.04	−136.59	−143.36	−145.09
Minimum potential energy		−265.47		−274.99	

[a]Calculations for triplet $An\cdot{}^4He_2$ represent the hypothetical two-fermion model system $An\cdot{}^4He_2$(hyp.) (see text).

genvalue difference of the $1A_g$ states in the S_1 and in the S_0 electronic state and is $-1.62\ cm^{-1}$ for $An\cdot{}^4He_1$ and $-1.90\ cm^{-1}$ for $An\cdot{}^3He_1$, i.e., the 0–0 band of the complex is red-shifted with respect to the one of the bare molecule. While the potential parameters were fitted such (Sec. II A) that the calculated spectral shift of the $An\cdot{}^4He_1$ complex are in accord with the experimental value[46] of $\delta=-1.6\ cm^{-1}$, the predicted value $\delta=-1.90\ cm^{-1}$ for $An\cdot{}^3He_1$ was not yet subjected to experimental scrutiny.

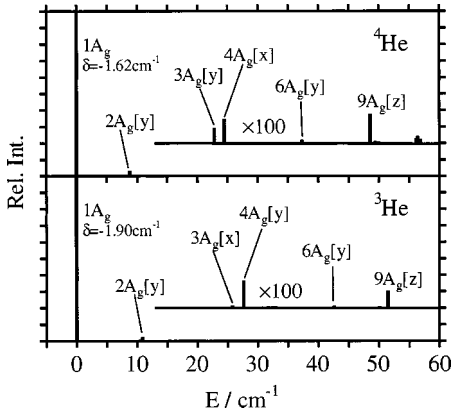

FIG. 4. The stick spectra of the calculated transition energies and Franck-Condon factors for the $An\cdot{}^4He_1$ and $An\cdot{}^3He_1$ complexes. The transition energies are given relative to that of the 0-0 vibronic line. The nature of the most prominent vibronic transitions are labeled by *x*, *y*, and *z*, and the term symbols of the corresponding excited states are given (only A_g series, since the B_{1u} series is quasidegenerate in the considered energy range up to 60 cm^{-1}).

The spectra of $An\cdot{}^4He_1$ and $An\cdot{}^3He_1$ do not show large isotope effects. The difference of the spectral shifts $\Delta\delta=\delta(^4He)-\delta(^3He)$ is only $\Delta\delta=0.28\ cm^{-1}$, and the gross pattern of the vibronic fine structure is also very similar. The main difference is the reverse order and intensity changes of the $[x]$ and the $[y]$ transition in the range 20–30 cm^{-1} (Fig. 4). Since both vibrational states have similar energies and are of the same symmetry type, a small perturbation such as the change of the kinetic energy integrals due to the mass effects has a marked effect on the wave functions.

Figures 5–7 exhibit the probability densities $P(x,y)$ of the helium atom on the molecular surface for some selected states,

$$P(x,y)=\int_{-\infty}^{\infty}dz\Psi^2(x,y,z), \tag{19}$$

i.e., the $P(x,y)$ are probability densities projected on the molecular plane. Figures 5 and 6 show the vibrational ground state $1A_g$, the first excited state $1B_{2u}$, as well as some excited A_g states, which are involved in the most intense spectral transitions which were presented in Fig. 4. For each state, four panels are given in one row, depicting the densities for ^4He and ^3He either for the S_0 and for the S_1 state anthracene-helium potential. For the $1A_g$, $1B_{2u}$, and $2A_g$ states, Fig. 5, the differences originating from different isotopes and potentials are only minor for the low-lying

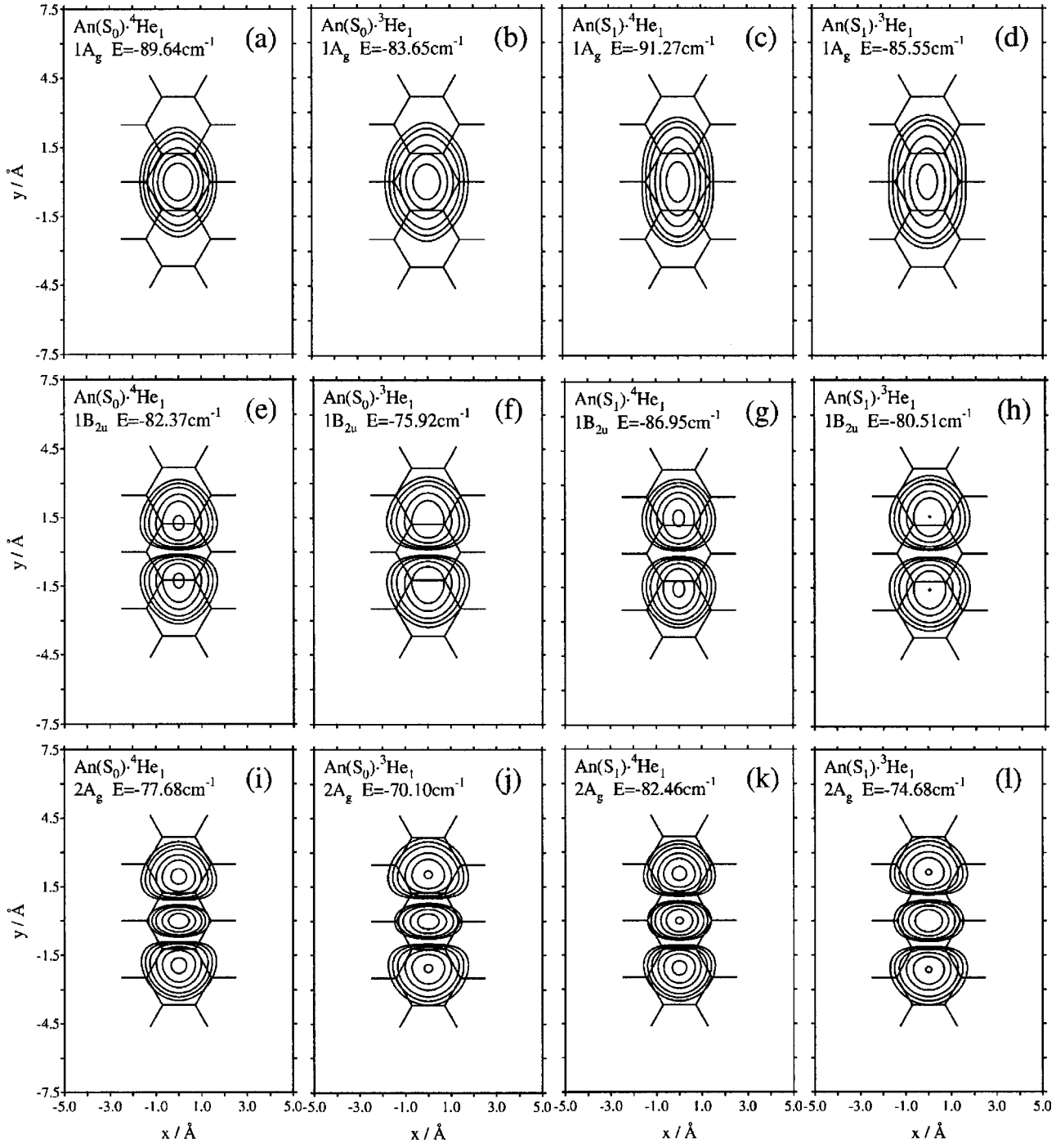

FIG. 5. Contour plots of the probability density of the helium atom on the anthracene molecular surface for the vibrational ground state $1A_g$ (a)–(d), the first vibrationally excited state $1B_{2u}$ (e)–(h), and the $2A_g$ state (i)–(l). For each state, four panels are given to show the differences between the potential energy surfaces and isotopes. Contour lines are given for density values of 0.005, 0.01, 0.02, 0.05, 0.10, and 0.20.

states. As a general trend, the densities of the ^{3}He atom are somewhat more extended on the molecular surface than of the ^{4}He atom, as expected. In addition, in the S_1 state the densities of both ^{4}He and ^{3}He are somewhat shifted towards the outer rings of the anthracene molecule, since the bottom of the S_1 state potential basin reaches farther into the outer rings than of the S_0 state potential (Fig. 1). The densities among of the $3A_g$ and $4A_g$ states of the S_1 state potential exhibit larger isotope differences [Figs. 6(c), 6(d), 6(g), and 6(h)], in correspondence with the intensity change of their spectral bands, Fig. 3.

The $8A_g$ and $9A_g$ states depicted in Figs. 6(i)–6(l) assume higher 1D z quantum numbers, mainly $\mu_z=1$. Their linear-expansion coefficients are $0.89\phi_{001}-0.17\phi_{002}$ for the $9A_g$ state of An$(S_0)\cdot{}^4$He$_1$, $0.79\phi_{001}-0.31\phi_{002}$ for the $8A_g$ state of An$(S_0)\cdot{}^3$He$_1$, $0.80\phi_{001}-0.21\phi_{002}$ for the $9A_g$ state of An$(S_1)\cdot{}^4$He$_1$, and $0.75\phi_{001}-0.35\phi_{002}$ for the $9A_g$ state of An$(S_1)\cdot{}^3$He$_1$. These states consist mainly of basis functions with $\mu_x=0$ and $\mu_y=0$ and show therefore only little nodal structure in the xy plane. Figure 8 shows the density profiles $P(z)$,

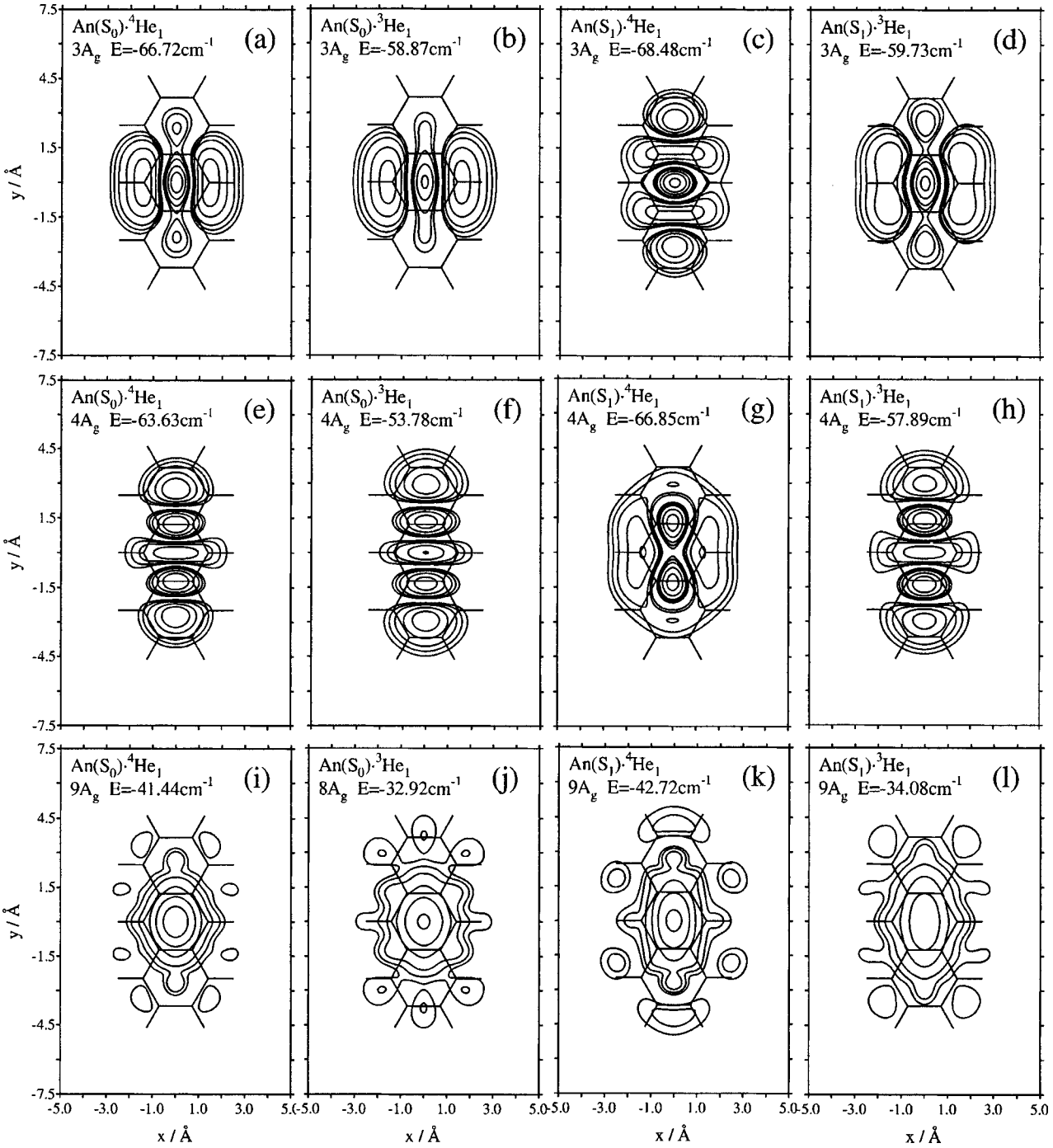

FIG. 6. Contour plots of the probability density of the helium atom on the anthracene molecular surface for the $3A_g$ (a)–(d), the $4A_g$ (e)–(h) and the $9A_g$ state (i)–(l) for the two potentials and helium masses. For the S_0 state potential of $An\cdot{}^3He_1$, panel (j), the density of the $8A_g$ state is given due to the reverse order of the vibrational states. Contour lines are given for density values of 0.005, 0.01, 0.02, 0.05, 0.10, and 0.20.

$$P(z)=\int_{\infty}^{-\infty}dx\int_{\infty}^{-\infty}dy\Psi^2(x,y,z), \tag{20}$$

of the vibrational states of the $An\cdot{}^4He_1$ complex presented in Figs. 5–7. While the lower states, Figs. 8(a)–8(d), have a density profile $P(z)$ which is an asymmetrically distorted Gaussian with a maximum at 3.2 Å (the equilibrium distance of the He atom to the molecular plane is 3.10 Å for the S_0 and 3.15 Å for the S_1 state potential), the density profile of the $9A_g$ state is bimodal, reflecting the node of the $\mu_z=1$ function.

Of particular interest is the question, how much the probability densities must be expanded into space to lift the degeneracy between the A_g and the B_{1u} states. Figure 7 exhibits three examples for the probability densities $P(x,y)$ of higher excited states, of the $12A_g$ and of the $18A_g$ state of the $An(S_0)\cdot{}^4He_1$ and of the $13A_g$ state of the $An(S_0)\cdot{}^3He_1$ complex. For the $12A_g$ state [panel (a) of Fig. 7], the density reaches somewhat beyond the peripheral H atoms (note that the van der Waals radii of the H atoms exceed the molecular frames drawn in the figures), but no splitting is observed.

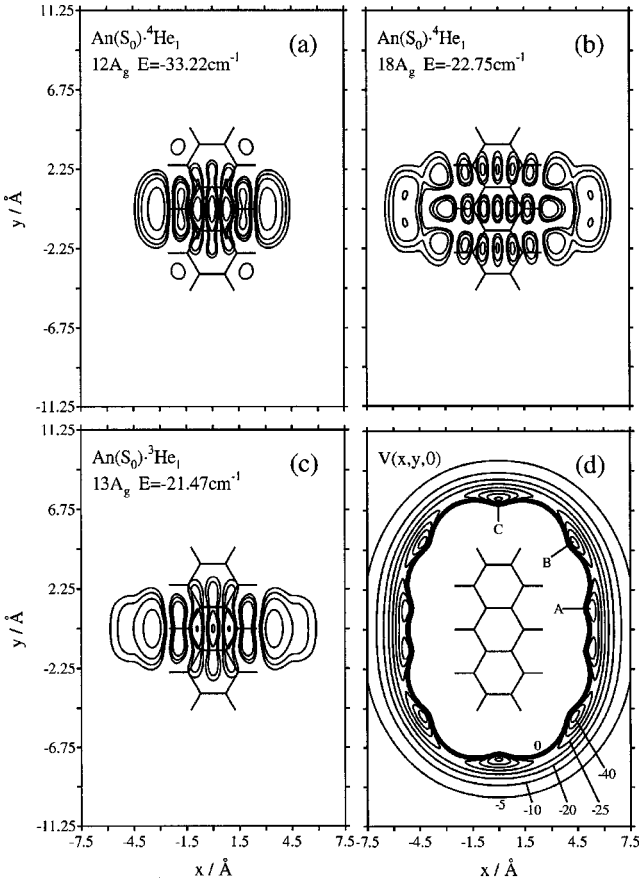

FIG. 7. The possibility of side crossing for higher excited vibrational states of the An$(S_0)\cdot$He$_1$ complex. The contour plots of the probability density of the (a) $12A_g$ and (b) of the $18A_g$ state of the An$(S_0)\cdot 4$He$_1$ complex as well as (c) of the $13A_g$ state of the An$(S_0)\cdot{}^3$He$_1$ complex are compared with a contour map (d) of the PES in the *xy* plane. Contour lines are given for density values of 0.005, 0.01, 0.02, and 0.05 [panels (a)–(c)] and for potential-energy values of -5, -10, -20, -25, and -40 cm^{-1}. The potential-energy surface has ten first-order saddle points, which by symmetry fall into three classes A, B, and C. Their potential-energy values are -44.7, -42.6, and -40.9 cm^{-1}, respectively. Unlike the $12A_g$ state [panel (a)] the $18A_g$ and the $13A_g$ state [panels (b) and (c)] have considerable densities in the regions of saddle point A and exhibit a notable energy splitting with respect to the corresponding nB_{1u} states.

The $18A_g$ state [panel 7(b)] is the lowest A_g state which shows the A_g/B_{1u} energy splitting for the An$(S_0)\cdot{}^4$He$_1$ complex; the $18A_g$ state has an energy eigenvalue of -22.75 cm^{-1} and is by 0.09 cm^{-1} lower in energy than the $18B_{1u}$ state. Although for the An$(S_0)\cdot{}^3$He$_1$ complex an appreciable splitting (0.04 cm^{-1}) is exhibited already for the $13A_g$ state [panel (c)], the splitting occurs at about the same energy (-21.47 cm^{-1}) as for the An$(S_0)\cdot{}^4$He$_1$ complex. In order to conclude whether the A_g/B_{1u} splitting is due to tunneling or to side crossing, the energy eigenvalues have been related to the potential barriers of side crossing. There are ten saddle points in the *xy* plane characterized by one imaginary frequency and a corresponding vibration in *z* direction. Panel (d) of Fig. 7 shows a contour map of the potential energy in the *xy* plane. Due to symmetry the ten saddle points are grouped into three classes, marked as A, B, and C in panel 7(d). Their potential energies are -44.7, -42.6, and -40.9 cm^{-1}, respectively. Since notable splitting occurs only for states above the saddle-point potential energies, the splitting

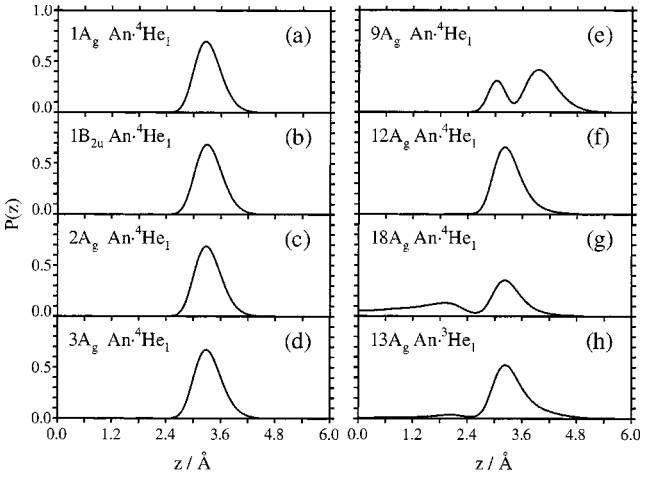

FIG. 8. The density profiles $P(z)$ of some densities given in Figs. 5–7.

corresponds to classical side crossing rather than to tunneling. Comparing the spatial extension of the probability densities to the locations of the saddle points, only the $18A_g$ state of the An$(S_0)\cdot{}^4$He$_1$ complex [panel 7(b)] and the $13A_g$ state of the An$(S_0)\cdot{}^3$He$_1$ state assume appreciable values at the saddle points A. Moreover, the spacing of the potential-energy contour lines show a steep increase of the potential energy towards the molecule; the innermost contour line already corresponds to zero potential energy. The density of the $12A_g$ state is inside the region of high potential energy in the *xy* plane, in accord with the absence of a notable A_g/B_{1u} energy splitting. The contour map of the S_1 state potential-energy surface (PES) in the molecular plane (not shown in Fig. 7) resembles very much the one of the S_0 state [Fig. 7(d)]. The locations of the saddle points deviate only by $\approx$0.01 Å compared to those of the S_0 state. The potential energies are -47.6, -45.3, and -45.6 cm^{-1} for the saddle points A, B, and C, respectively.

The density profiles $P(z)$ of the $12A_g$ and of the $18A_g$ state of the An$(S_0)\cdot{}^4$He$_1$ complex as well as the density of the $13A_g$ state of the An$(S_0)\cdot{}^3$He$_1$ complex are included in Fig. 8 [panels (g) and (h)]. Especially the $18A_g$ state [Fig. 8, panel (g)] shows a large density of $P(0)=0.055$ in the *xy* plane, the $13A_g$ state of An$(S_0)\cdot{}^3$He$_1$ a value of $P(0)=5.5\times10^{-3}$, which is still appreciable. In Fig. 9(a) the densities $P(0)$ [i.e., the density profile values $P(z)$ at $z=0$] are plotted vs the eigenvalues of the corresponding states. For both An$(S_0)\cdot{}^4$He$_1$ and An$(S_0)\cdot{}^3$He$_1$, a marked increase of $P(0)$ takes place at ≈-22 cm^{-1}, in accord with the statement made above regarding the onset of A_g/B_{1u} splitting, while below this energy threshold $P(0)$ assumes values $<10^{-6}$. Below ≈-22 cm^{-1}, where the energy splitting A_g/B_{1u}, B_{2u}/B_{3g}, etc. is negligible ($\leqslant$0.01 cm^{-1}), the corresponding wave-function pairs $\psi(nA_g)/\psi(nB_{1u})$, $\psi(nB_{2u})/\psi(nB_{3g})$, etc. are distinguished only by their nodal behavior with respect to the *xy* plane but otherwise identical. Above the energy threshold of ≈-22 cm^{-1}, the mixing of the one-sided C_{2v} wave functions becomes excessive, so that the resulting wave-function pairs $\psi(nA_g)/\psi(nB_{1u})$, $\psi(nB_{2u})/\psi(nB_{3g})$, etc. within the D_{2h} framework show no or only little similarities. Consequently, the energy splitting

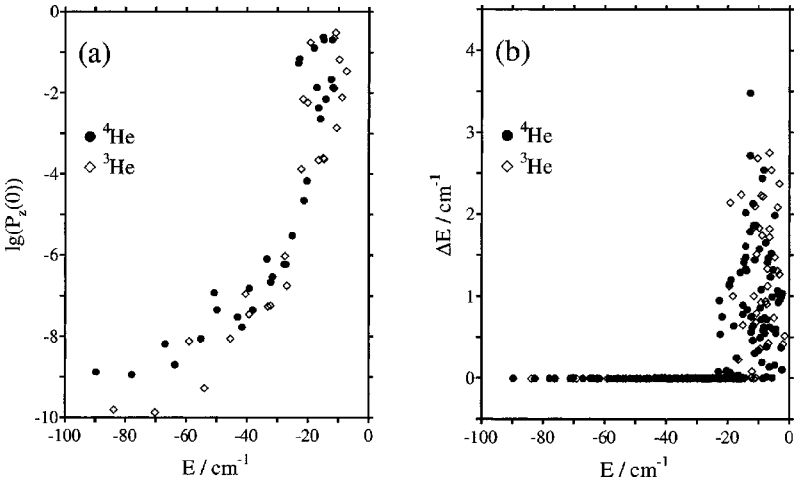

FIG. 9. The ability of side crossing and the corresponding energy splitting for the $An(S_0)\cdot{}^4He_1$ and for the $An(S_0)\cdot{}^3He_1$ complex as a function of the state energy E. (a) The probability density $P(z)$ of the He atom in the xy plane of the molecule. (b) The energy splittings $\Delta E=|E(nA_g)-E(nB_{1u})|$, $\Delta E=|E(nB_{2u})-E(nB_{3g})|$, $\Delta E=|E(nB_{1g})-E(nA_u)|$, and $\Delta E=|E(nB_{3u})-E(nB_{2g})|$ as a consequence of the interaction of the one-particle densities on both sides of the aromatic molecule. The onset of a notable energy splitting is at ≈ -22 cm^{-1}.

ΔE can be taken only by comparing the eigenvalues, i.e., $\Delta E=|E(nA_g)-E(nB_{1u})|$, $\Delta E=|E(nB_{2u})-E(nB_{3g})|$, $\Delta E=|E(nB_{1g})-E(nA_u)|$, and $\Delta E=|E(nB_{3u})-E(nB_{2g})|$. In Fig. 9(b) the energy splittings ΔE are plotted versus the energy eigenvalues. The splittings ΔE are negligibly small (less than 0.01 cm^{-1}) in the range $E=-90-\approx -22$ cm^{-1}, while at the onset ≈ -22 cm^{-1} a sharp rise of ΔE is manifested, reaching at most 3–4 cm^{-1}. No pronounced isotope effects on ΔE could be identified.

Comparing the results obtained from various basis sets and assessing the basis set convergence, the small basis set A consisting of 54 A_g symmetry-adapted 3D basis functions leads to an energy of -89.59 cm^{-1} for the vibrational ground state of the $An(S_0)\cdot{}^4He_1$ complex, while the large basis set C of 1080 A_g symmetry-adapted basis function gives an energy of -89.64 cm^{-1}, only by 0.05 cm^{-1} lower than basis set A. This means that for the vibrational ground state, energy convergence is already almost achieved for basis set A. In our previous paper[47] we have used basis set A throughout to calculate the eigenstates of the (1|0) and of the (2|0) complex up to an energy of 50 cm^{-1} above the ground state. This was the relevant spectroscopic energy range, for which spectroscopic assignments have been made. In addition to the excellent agreement between calculated and experimentally observed transition energies already addressed in our previous paper,[47] we can assess now the accuracy of basis set A, taking the large basis set C as the ''true'' reference. Within the energy range of 50 cm^{-1} above the ground state, the deviation of the energies of basis set A is mostly not larger than 0.3 cm^{-1} and at most 0.83 cm^{-1} for the $10A_g$ state. That is to say, basis set A is a small and very efficient basis set in the energy range up to $\approx$50 cm^{-1}.

The intermediate basis set B, which is an extension of basis set A up to 1D quantum numbers $\mu_x=8$, $\mu_y=18$, and $\mu_z=3$ and which consists of 200 symmetry-adapted 3D basis functions, leads to the converged ground-state energy of -89.64 cm^{-1} and its accuracy is better than 0.17 cm^{-1} up the $17A_g$ state (-25.08 cm^{-1}). For higher states, for which splitting due to the interaction of the densities on both sides of the molecule becomes important, basis set B is insufficient because of its lack of functions in the molecular plane and at the molecular periphery. As the density plots showed, functions in the molecular plane are essential to describe these states. It also turned out that the splitting can be described only, if 1D functions are added which reach farther into space than $\mu_x=8$, $\mu_y=18$. Although our large basis set C is augmented by additional Gaussians in the molecular plane and in the molecular periphery beyond $\mu_x=8$, $\mu_y=18$, it remains to be established by further work to what extent these higher-lying states are quantitatively converged.

B. Anthracene·He$_2$

Two isomers exist for $An\cdot He_2$, the two-sided (1|1) and the one-sided (2|0) isomer. The (1|1) isomer represents the global minimum on the $An\cdot He_2$ potential-energy surface (PES). Its minimum potential energy is -276.35 cm^{-1} for the anthracene S_0 state potential. This value is only by 0.15 cm^{-1} lower than twice the value of the $An(S_0)\cdot He_1$ (1|0) complex, indicating that the two helium atoms very weakly interact. The PES of the (2|0) isomer has a symmetric double minimum with two well depths of -265.47 cm^{-1}, where in each minimum the nuclear configurations assume C_s symmetry. Both minimum nuclear configurations are related by a $C_2(z)$ symmetry operation, with the coordinates of the He atoms of one of the configurations being $x_1=x_2=0$, $y_1=-0.4110$ Å, $y_2=2.3308$ Å, $z_1=3.1088$ Å, $z_2=3.1092$ Å. Both minima are interconnected by a first-order saddle point, which has a potential energy of -258.77 cm^{-1} and in which the nuclear configuration assumes C_{2v} symmetry.

Since the (1|1) isomer can be viewed to a good approximation as a doubled (1|0) complex, we have focused on the more interesting (2|0) isomer. Also, as discussed below, the (2|0) isomer is an essential building block of the $An\cdot He_3$ and $An\cdot He_4$ clusters. In order to sort out permutation symmetry and mass effects, we have calculated the singlet and triplet states for particles of mass 3 and of mass 4. That is to say, we have calculated the singlet and the triplet states of the two-fermion system $An\cdot{}^3He_2$ and of a hypothetical model system with two fermions of mass 4, denoted as $An\cdot{}^4He_2$(hyp.). In addition, we present our results for the two-boson $An\cdot{}^4He_2$ system. In Sec. II B, we presented the details of the calculations of the triplet states of fermions and of singlet states of fermions and bosons, where we note that two bosons of spin 0 have the same CI matrix elements as two fermions of spin

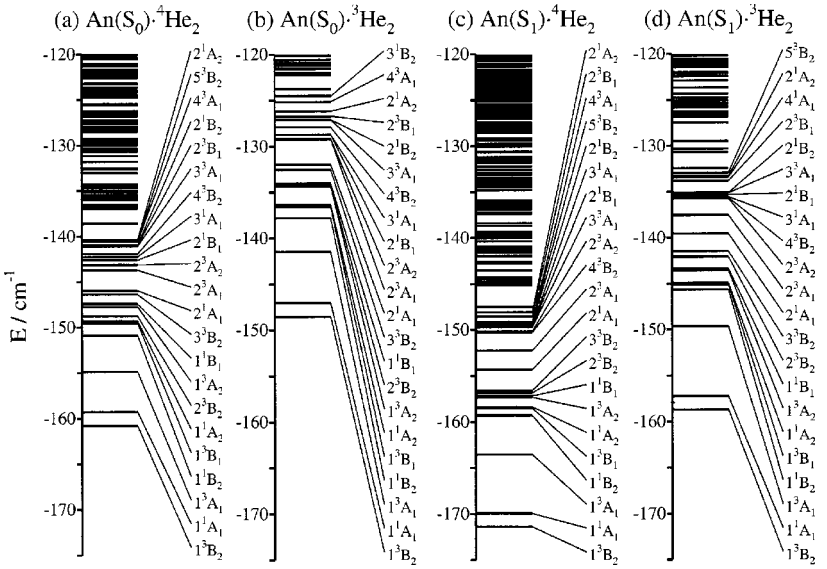

FIG. 10. The vibrational level diagrams for the two-boson An·^{4}He$_2$ and for the two-fermion An·^{3}He$_2$ complex in the S_0 and in the S_1 electronic states of the anthracene molecule. For An·^{4}He$_2$ the triplet state energies of a hypothetical two-fermion system An·^{4}He$_2$(hyp.) of mass 4 have been included.

$\frac{1}{2}$ in a singlet state and therefore behave identically. All calculations for An·^{3}He$_2$, An·^{4}He$_2$ and the hypothetical model system An·^{4}He$_2$(hyp.) were carried out for the single-sided (2|0) isomer (C_{2v} symmetry), using the small basis set A. In Fig. 10 the eigenvalue spectra are depicted for the S_0 and the S_1 state anthracene-helium potentials. In addition, the energy eigenvalues are summarized in Table I for the lowest energy eigenvalue for each multiplicity and symmetry. Figure 10 and Table I contain also the energy eigenvalues of the triplet states of two hypothetical fermions of mass 4, An·^{4}He$_2$(hyp.). In the two-fermion systems An·^{3}He$_2$ and An·^{4}He$_2$(hyp.) we found that for both particle masses and for both anthracene-helium potentials, a triplet $^3B_2$ state is always the vibrational ground state (Fig. 10), while the first singlet state (1^1A_1) is $\approx$1.5 cm^{-1} above it (Table I). Taking the minimum potential energy of -265.47 cm^{-1}, the zero point energy ε_0 is 106.19 cm^{-1} for the ground 1^1A_1 state of An(S_0)·^{4}He$_2$ and 116.95 cm^{-1} for the ground 1^3B_2 state of the An(S_0)·^{3}He$_2$ complex. The isotope effect $\Delta\varepsilon_0/\varepsilon_0$ is only $\approx$10%, manifesting a partial cancellation of mass and permutation symmetry effects. From the eigenvalues listed in Table I, one can also infer the energies D for the dissociation process An·He$_2$$\rightarrow$An·He$_1$+He. The dissociation energies are 69.6 cm^{-1} for An(S_0)·^{4}He$_2$, 64.8 cm^{-1} for An(S_0)·^{3}He$_2$, 80.1 cm^{-1} for An(S_1)·^{4}He$_2$, and 73.1 cm^{-1} for An(S_1)·^{3}He$_2$. The isotope effects in the dissociation energies D reveal values which are higher for the heavy isotope, in contrast to the ε_0 values which are lower for the heavy isotope. The isotope effects on D involve the difference between mass and permutation symmetry contributions for An·He$_2$ and mass effects for An·He$_1$.

Having electronic structure calculations of atoms in mind, it is interesting to find a triplet state as the ground state of two fermions in nondegenerate spatial orbitals. As it will be shown in the following, this fact manifests the dominance of the He-He two-particle repulsion over the one-particle interactions. In Table II the eigenvalues and the main CI expansion coefficients of several singlet and triplet states of the An(S_0)·^{3}He$_2$ cluster are listed. In order to study the singlet-triplet splitting and the effect of the He-He repulsion on the wave functions and energies, we have performed also CI calculations for An·^{3}He$_2$ in which all two-particle integral values have been scaled down by a uniform numerical value, i.e., by a factor of 10^3, 10^4, and 10^5. The first column of Table II contains the CI results for genuine unscaled two-particle integral values, i.e., for a scaling factor of 1. With decreasing the two-particle integral values, the energy eigenvalues of all states drop, but for the singlet states the energy decreases more than for the triplet states. When the two-particle integrals are scaled down by a factor of 10^3, a crossover between the 1^1A_1 and the 1^3B_2 state takes place and the 1^1A_1 state forms the ground state.

Singlet-triplet splitting is defined as the energy difference between the singlet and the triplet state of the same orbital configuration. However, the singlet and triplet states listed in Table II show an extensive configuration mixing, so that similarities in orbital configurations cannot be determined. Only when the two-particle integrals are scaled down by a factor of at least 10^4, the configurational mixing is reduced such that the correspondences between the 1^3A_1 and the 2^1A_1 as well as between the 1^3B_2 and the 1^1B_2 states become clearly apparent. Based on these correspondences, one can also assign the values for the singlet-triplet splitting in the CI calculations of the unscaled two-particle integral values. For An(S_0)·^{3}He$_2$, the singlet-triplet splitting is 9.5 cm^{-1} between the 1^3A_1 and 2^1A_1 states and 10.7 cm^{-1} between the 1^3B_2 and 1^1B_2 states.

The configuration interaction leads to admixtures of higher 1D quantum numbers, which for the lowest singlet and triplet states involves solely higher 1D quantum numbers μ_y, while higher excited states also show large participation of 1D quantum states $\mu_x>0$ and $\mu_z>0$. Configurational mixing is generally not less marked for triplet than for singlet states. In the one-configuration approximation, i.e., in the complete absence of configurational mixing, the singlet-triplet splitting assumes the value of twice the exchange integral K_{12}. In this context it is instructive to consider the values of some two-particle integrals, also to convey a gen-

TABLE II. Energies and main CI expansion coefficients of the wave functions of some singlet and triplet states of the An(S_0)$\cdot{}^3$He$_2$ complex and their dependence on the two-particle integral values. The integral scaling factor given in the first row specifies the numerical factor, by which all two-particle integral values have been divided, e.g., the first column of the integral scaling factor 1 contains the results of the CI calculation for the unscaled integral values.

Integral scaling factor	1	10^3	10^4	10^5
1^1A_1	-147.0 cm^{-1}	-157.8 cm^{-1}	-163.7 cm^{-1}	-166.8 cm^{-1}
$\Delta(\phi_{000},\phi_{000})$		0.55	0.86	0.93
$\Delta(\phi_{020},\phi_{000})$	-0.43	0.60	0.31	
$\Delta(\phi_{200},\phi_{000})$		0.24	0.22	
$\Delta(\phi_{001},\phi_{000})$			-0.23	-0.23
$\Delta(\phi_{010},\phi_{010})$	0.50	-0.38		
$\Delta(\phi_{030},\phi_{010})$	0.39			
$\Delta(\phi_{020},\phi_{020})$	-0.43			
1^3A_1	-141.5 cm^{-1}	-151.4 cm^{-1}	-153.9 cm^{-1}	-153.7 cm^{-1}
$\Delta(\phi_{020},\phi_{000})$	-0.40	0.89	0.89	0.93
$\Delta(\phi_{040},\phi_{000})$	-0.48	0.25	0.25	
$\Delta(\phi_{060},\phi_{000})$	-0.27			
$\Delta(\phi_{030},\phi_{010})$	0.49			
$\Delta(\phi_{050},\phi_{010})$	0.26			
2^1A_1	-132.0 cm^{-1}	-146.1 cm^{-1}	-151.5 cm^{-1}	-153.4 cm^{-1}
$\Delta(\phi_{000},\phi_{000})$		0.33	-0.29	
$\Delta(\phi_{020},\phi_{000})$		-0.25	0.76	0.89
$\Delta(\phi_{040},\phi_{000})$	0.36			
$\Delta(\phi_{060},\phi_{000})$	0.36			
$\Delta(\phi_{200},\phi_{000})$		0.42		
$\Delta(\phi_{010},\phi_{010})$		0.41	-0.33	
$\Delta(\phi_{020},\phi_{020})$	-0.37	-0.35		
$\Delta(\phi_{030},\phi_{010})$		0.33		
$\Delta(\phi_{040},\phi_{020})$	-0.27			
$\Delta(\phi_{030},\phi_{030})$	0.33			
$\Delta(\phi_{120},\phi_{100})$		-0.26		
1^3B_2	-148.5 cm^{-1}	-157.1 cm^{-1}	-159.1 cm^{-1}	-159.5 cm^{-1}
$\Delta(\phi_{010},\phi_{000})$	-0.37	0.85	0.92	0.92
$\Delta(\phi_{030},\phi_{000})$	-0.34			
$\Delta(\phi_{020},\phi_{010})$	0.70	-0.28		
$\Delta(\phi_{030},\phi_{020})$	-0.22			
1^1B_2	-137.8 cm^{-1}	-152.0 cm^{-1}	-156.8 cm^{-1}	-159.2 cm^{-1}
$\Delta(\phi_{010},\phi_{000})$	0.23	0.70	0.89	0.92
$\Delta(\phi_{030},\phi_{000})$	0.53	0.55	0.25	
$\Delta(\phi_{050},\phi_{000})$	0.38			
$\Delta(\phi_{020},\phi_{010})$	-0.29			
$\Delta(\phi_{030},\phi_{020})$	0.24			
$\Delta(\phi_{040},\phi_{010})$	-0.38			

eral impression of their magnitude in these systems. In Table III the values of some two-particle integrals are listed. They are mainly in the range 10^4-10^5 cm^{-1}, typically 10^2-10^3 times higher than the one-particle integrals. In Table IV the singlet-triplet splitting of the 1^3A_1-2^1A_1 and of the 1^3B_2-1^1B_2 states are confronted with the values of the corresponding exchange integrals. The results in Table IV show that the two-particle integrals have to be reduced by a factor of 10^4-10^5 until the singlet-triplet splitting scales linearly with the exchange integral and comes close to twice of its value. Accordingly, simple one-configuration approximations are insufficient to handle the problem of the An$\cdot{}^3$He$_2$ two-fermion system.

Figure 11 shows how the one-particle densities $P(x,y)$ of the lowest singlet and triplet states of the An(S_0)$\cdot{}^3$He$_2$ complex vary with the magnitude of the two-particle integrals. For a two-fermion system, the one-particle densities $P(x,y)$ projected on the x,y plane are given by

TABLE III. The values of some two-particle integrals.

Integral	Value/cm^{-1}	Integral	Value/cm^{-1}
$(\phi_{000}\phi_{000}\|\phi_{000}\phi_{000})$	71 745	$(\phi_{020}\phi_{000}\|\phi_{020}\phi_{000})$	12 457
$(\phi_{010}\phi_{000}\|\phi_{010}\phi_{000})$	19 928	$(\phi_{020}\phi_{010}\|\phi_{010}\phi_{000})$	11 789
$(\phi_{010}\phi_{010}\|\phi_{000}\phi_{000})$	29 579	$(\phi_{020}\phi_{010}\|\phi_{020}\phi_{010})$	25 337
$(\phi_{010}\phi_{010}\|\phi_{010}\phi_{010})$	39 254	$(\phi_{020}\phi_{020}\|\phi_{000}\phi_{000})$	19 084
$(\phi_{020}\phi_{000}\|\phi_{000}\phi_{000})$	-20 031	$(\phi_{020}\phi_{020}\|\phi_{010}\phi_{010})$	31 342
$(\phi_{020}\phi_{000}\|\phi_{010}\phi_{010})$	5 301	$(\phi_{020}\phi_{020}\|\phi_{020}\phi_{020})$	37 642

TABLE IV. Two examples for the singlet-triplet splitting of the An(S_0) $\cdot{}^3$He$_2$ complex. The singlet-triplet splitting between the 2^1A_1 and the 1^3A_1 as well as between the 1^1B_2 and the 1^3B_2 state is given as a function of the magnitude of the two-particle integrals as expressed by the integral scaling factor, by which all two-particle integrals involved in the CI calculation have been scaled down uniformly (the scaling factor of 1 means no scaling). The singlet-triplet splitting is compared with the value twice the corresponding exchange integral (also scaled down by the same factor).

Integral scaling factor	1	10^3	10^4	10^5
$E(2^1A_1)-E(1^3A_1)/\mathrm{cm}^{-1}$	9.5	5.3	2.4	0.25
$2(\phi_{020}\phi_{000}\|\phi_{020}\phi_{000})/\mathrm{cm}^{-1}$	2.49×10^4	24.9	2.5	0.25
$E(1^1B_2)-E(1^3B_2)/\mathrm{cm}^{-1}$	10.7	5.1	2.3	0.32
$2(\phi_{010}\phi_{000}\|\phi_{010}\phi_{000})/\mathrm{cm}^{-1}$	3.99×10^4	39.9	4.0	0.40

$$P(x,y)=2\int_0^\infty dz_1\int_{-\infty}^\infty dx_2\int_{-\infty}^\infty dy_2\int_{-\infty}^\infty dz_2\int ds_1\int ds_2 \times\Psi^2(x_1,y_1,z_1,s_1,x_2,y_2,z_2,s_2) \tag{21}$$

with s_1 and s_2 denoting the spin coordinates. The numerical-factor of 2 normalizes the density to two particles. The CI expansion of ψ^2 consists of products of configurations. The contribution of a product ${}^1\Delta_1(\mu,\mu)\cdot{}^1\Delta_1(\nu,\nu)$ of two type-1 singlet configurations to the one-particle density is given by

$$2\int d\tau_2\int ds_1\int ds_2\,{}^1\Delta_1(\mu,\mu)\,{}^1\Delta_1(\nu,\nu) =2\phi_\mu(1)\phi_\nu(1)\delta_{\mu\nu}, \tag{22}$$

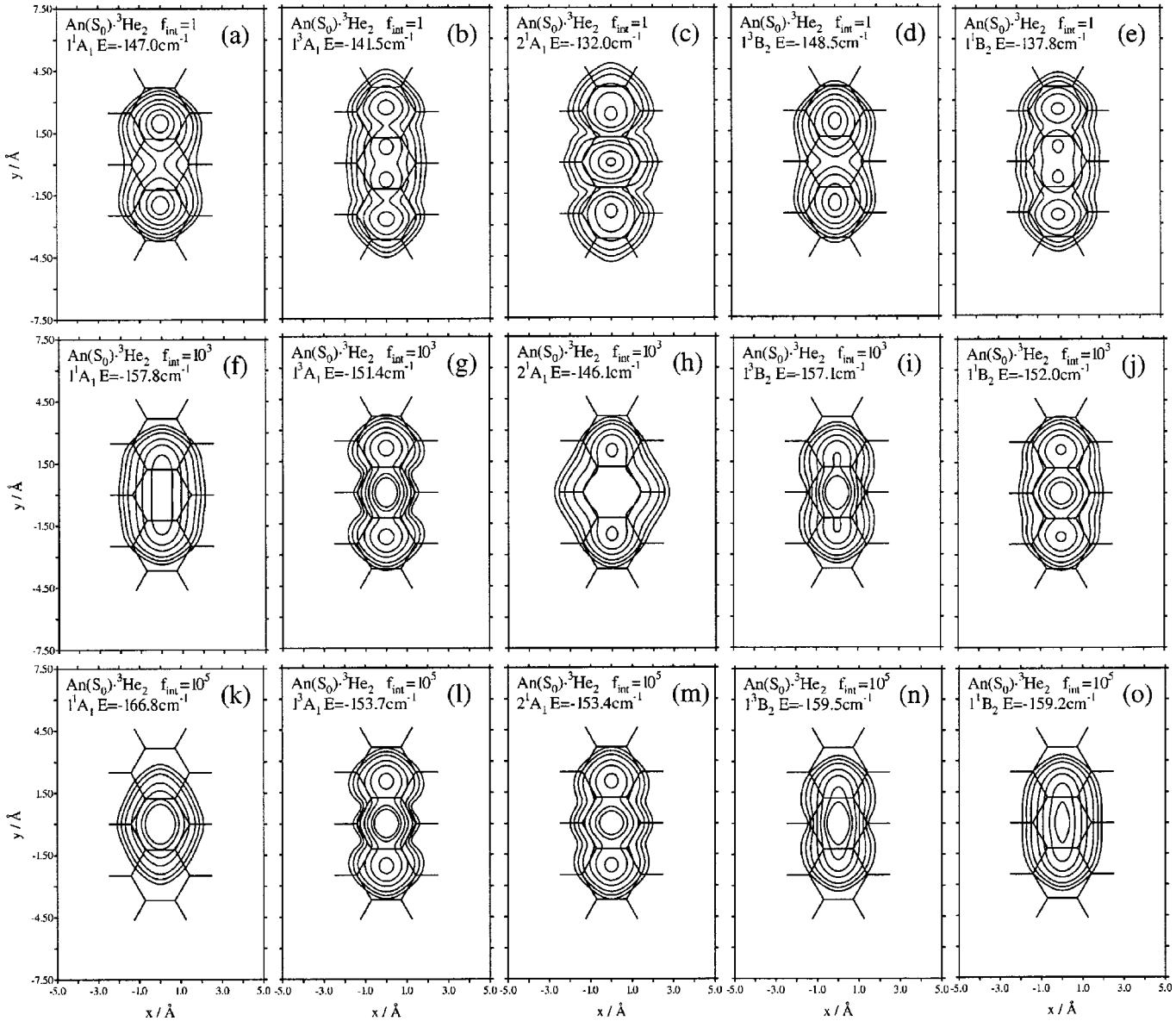

FIG. 11. The dependence of the one-particle densities on the magnitude of the two-particle integrals. Contour plots of the one-particle density $P(x,y)$, Eq. (21), are given for the 1^1A_1, 1^3A_1, 2^1A_1, 1^3B_2, and for the 1^1B_2 state of the two-fermion An(S_0)$\cdot{}^3$He$_2$ system. The first row [panels (a)–(e)] contain the CI calculation results in which all two-particle integrals kept their original values. In the CI calculations of panels (f)–(j) the values of all two-particle integrals have been scaled down by a numerical factor of $f_{\mathrm{int}}=10^3$, in the CI calculations of panels (k)–(o) by $f_{\mathrm{int}}=10^5$. Contour lines are given for density values of 0.005, 0.01, 0.02, 0.05, 0.10, 0.20, and 0.30.

of a product of type-1 type-2 configurations $^1\Delta_1(\mu,\mu)\cdot{}^1\Delta_2(\lambda,\sigma)$ by

$$2\int d\tau_2\int ds_1\int ds_2\,{}^1\Delta_1(\mu,\mu)^1\Delta_2(\lambda,\sigma)$$
$$=\sqrt{2}[\phi_\mu(1)\phi_\lambda(1)\delta_{\mu\sigma}+\phi_\mu(1)\phi_\sigma(1)\delta_{\mu\lambda}], \quad (23)$$

and of two singlet or triplet configurations $^{1,3}\Delta_2(\mu,\nu)\cdot{}^{1,3}\Delta_2(\lambda,\sigma)$ of type 2 by

$$2\int d\tau_2\int ds_1\int ds_2\,{}^{1,3}\Delta_2(\mu,\nu)\,{}^{1,3}\Delta_2(\lambda,\sigma)$$
$$=\phi_\mu(1)\phi_\lambda(1)\delta_{\nu\sigma}\pm\phi_\mu(1)\phi_\sigma(1)\delta_{\nu\lambda}$$
$$+\phi_\nu(1)\phi_\sigma(1)\delta_{\mu\lambda}\pm\phi_\nu(1)\phi_\lambda(1)\delta_{\mu\sigma}. \quad (24)$$

The minus signs on the right-hand side of Eq. (24) apply in case of triplet configurations.

The contour plots are given for the 1^1A_1, 1^3A_1, 2^1A_1, 1^3B_2, and the 1^1B_2 states (Fig. 11). The uppermost panels contain the CI calculation results of the unscaled integrals, the second and third row panels the CI calculations in which all two-particle integrals have been scaled down by a factor of 10^3 and 10^5, respectively. For the unscaled integrals, the contour plot of the 1^1A_1 state [panel (a)] has two density maxima on the outer rings of the anthracene molecule. The two density maxima correspond to the classical notion of two separated helium atoms. When the magnitude of the two-particle integrals is reduced, the maxima coalesce and the density maximum moves to the center of the molecular surface [panels (f) and (k)]. This is the consequence of the dominance of the configuration $\Delta(\phi_{000},\phi_{000})$, which assumes a CI expansion coefficient of 0.93, when all two-particle integrals are scaled down by a factor of 10^5 (Table II), so that the one-particle density approaches the value of $2\phi_{000}^2$ and the contour lines resemble those of the $An(S_0)\cdot{}^3He_1$ system, Fig. 5(b). When the values of the two-particle integrals are reduced, the densities of the 1^3A_1 and of the 1^1A_1 state as well as of the 1^3B_2 and of the 1^1B_2 state become similar, as the leading contribution to the densities of the 1^3A_1 and 2^1A_1 states become $\phi_{000}^2+\phi_{020}^2$ and to the densities of the states 1^3B_2 and 1^1B_2, i.e., $\phi_{000}^2+\phi_{010}^2$, cf. Table II.

Figure 12 exhibits the stick spectra of the transition energies and intensities of the $An\cdot He_2$ complexes, the singlet-singlet and triplet-triplet transitions of the two-boson $An\cdot{}^4He_2$ and of the two-fermion $An\cdot{}^3He_2$ system. The triplet-triplet transitions of a hypothetical two-fermion system of mass 4 have been also included [panel (b)]. Although the lowest singlet state is only 1.5 cm^{-1} above the triplet ground state for both $An\cdot{}^3He_2$ and $An\cdot{}^4He_2$(hyp.) (Fig. 10), the experimental temperature of 0.4 K does not allow for a notable thermal population of the singlet vibrational state in $An\cdot{}^3He_2$. This means that under the experimental conditions we can expect to observe only $1^3B_2\rightarrow n^3B_2$ transitions for $An\cdot{}^3He_2$ [panel (d) of Fig. 12]. Of course, the two-boson system $An\cdot{}^4He_2$ can assume only singlet states, so that only $1^1A_1\rightarrow n^1A_1$ transitions are possible [panel (a) in Fig. 12]. The main features of the four spectra look very similar, a strong 0-0 transition, a much weaker transition in the range

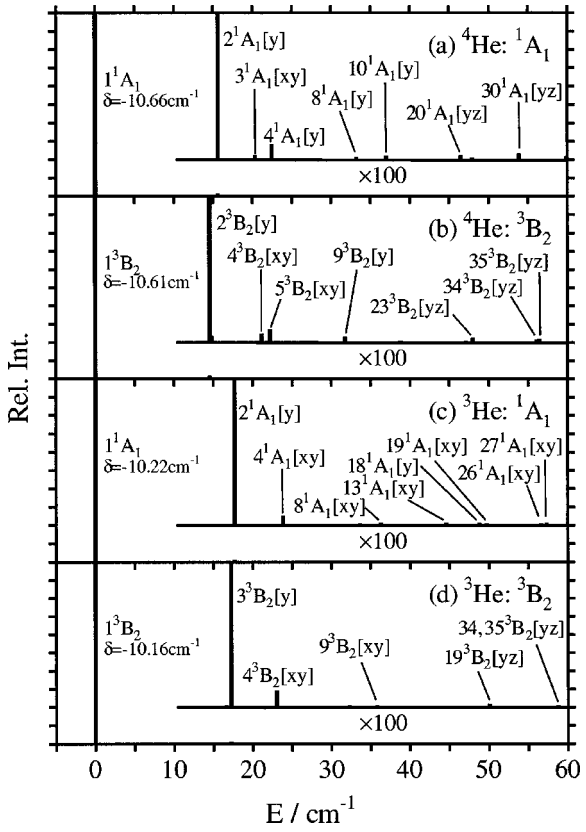

FIG. 12. The stick spectra of the calculated transition energies and Franck-Condon factors for the $An\cdot{}^4He_2$ and $An\cdot{}^3He_2$ complexes. (a) The $1^1A_1\rightarrow n^1A_1$ transitions of the two-boson $An\cdot{}^4He_2$ complex, (b) the $1^3B_2\rightarrow n^3B_2$ transitions of the hypothetical two-fermion system $An\cdot{}^4He_2$(hyp.), (c) the $1^1A_1\rightarrow n^1A_1$ transitions of the two-fermion $An\cdot{}^3He_2$ complex, (d) the $1^3B_2\rightarrow n^3B_2$ transitions of the two-fermion $An\cdot{}^3He_2$ complex. The transition frequencies are given relative to the position of the 0-0 transition. The numerical values of the red spectral shifts δ are marked at the 0-0 line. [x], [y], [z], [xy], etc. denote the nature of the transitions, i.e., the dominant change of the 1D functions with respect to the initial vibrational state.

14–17 cm^{-1}, and one or two [y] or [xy] transitions in the range 20–25 cm^{-1}. There are also many other, even weaker, transitions, which have been partly marked in Fig. 12. Looking at the two most intense vibronic bands of the $An\cdot{}^4He_2$ complex [Fig. 12(a)] and $An\cdot{}^3He_2$ [Fig. 12(d)], the isotope difference of the band positions is only 1.6 cm^{-1} between the $2^1A_1[y]$ and the $3^2B_2[y]$ transition and 0.6 cm^{-1} between the $4^1A_1[y]$ and the $4^3B_2[xy]$ transition. The similarity of the main spectral features may seem surprising in view of the different permutation symmetries and masses.

Figures 13 and 14 show contour plots of the one-particle densities $P(x,y)$, Eq. (21), for the $An\cdot He_2$ clusters. Figure 13 exhibits the densities of the four lowest $^1A_1$, Fig. 14 of the four lowest $^3B_2$ states. These states are the ones which also lead to the most prominent transitions in the spectra depicted in Fig. 12. The one-particle densities of the 1^3A_1 [Figs. 13(a)–13(d)] and of the 1^3B_2 [Fig. 14(a)–14(d)] states look very similar, although the wave functions of the 1^3B_2 states have a node in the xz plane. The densities of the $An\cdot{}^3He_2$ system are more extended into space than those of the $An\cdot{}^4He_2$ complex, as expected. The characterization of the wave functions in terms of [x] and [xy], as indicated in

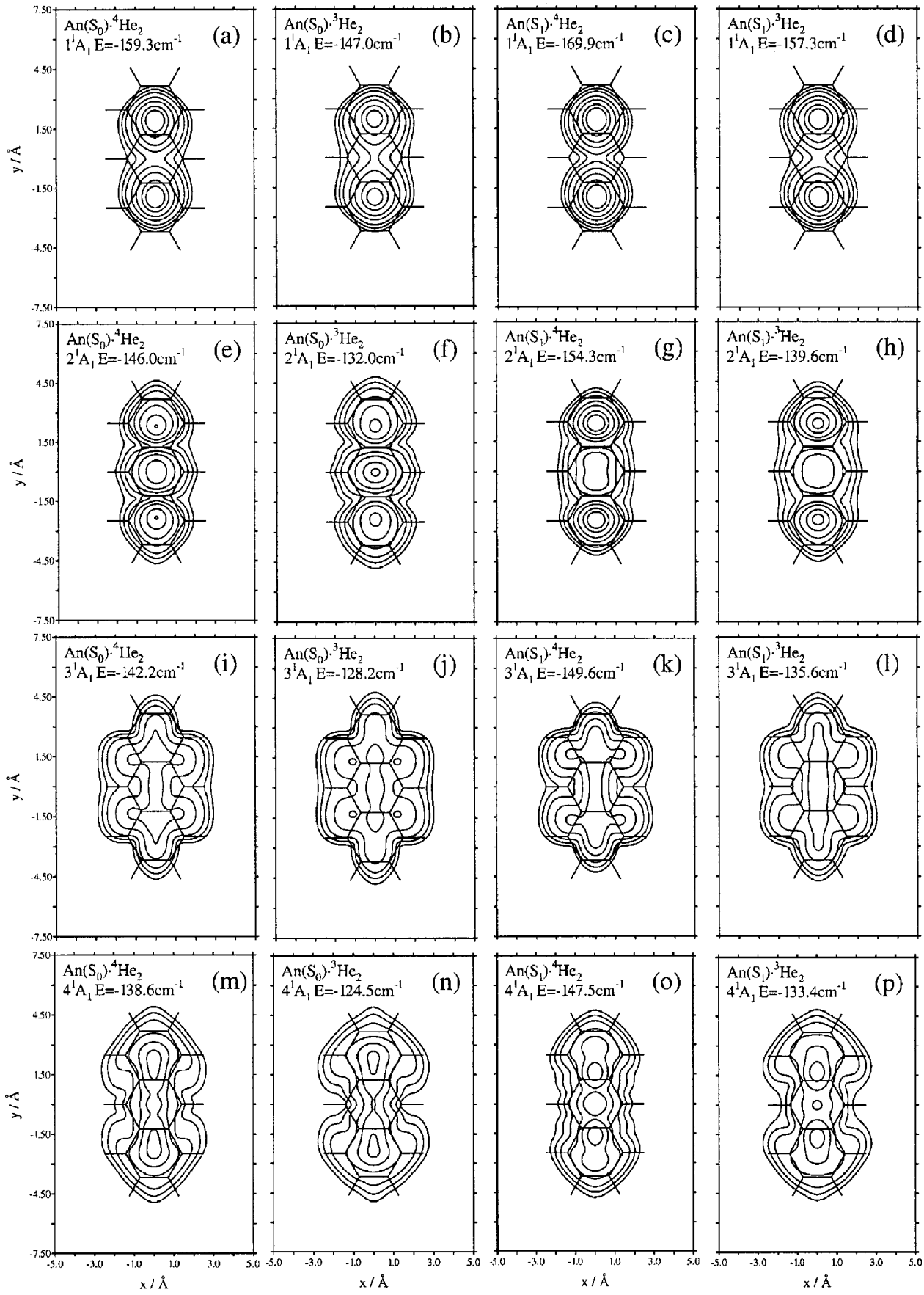

FIG. 13. Contour plots of the one-particle densities of the four lowest $^1A_1$ states of the An·^{4}He$_2$ and of the An·^{3}He$_2$ complexes for the S_0 and for the S_1 state anthracene-helium potential. Contour lines are given for density values of 0.005, 0.01, 0.02, 0.05, 0.10, 0.20, and 0.30.

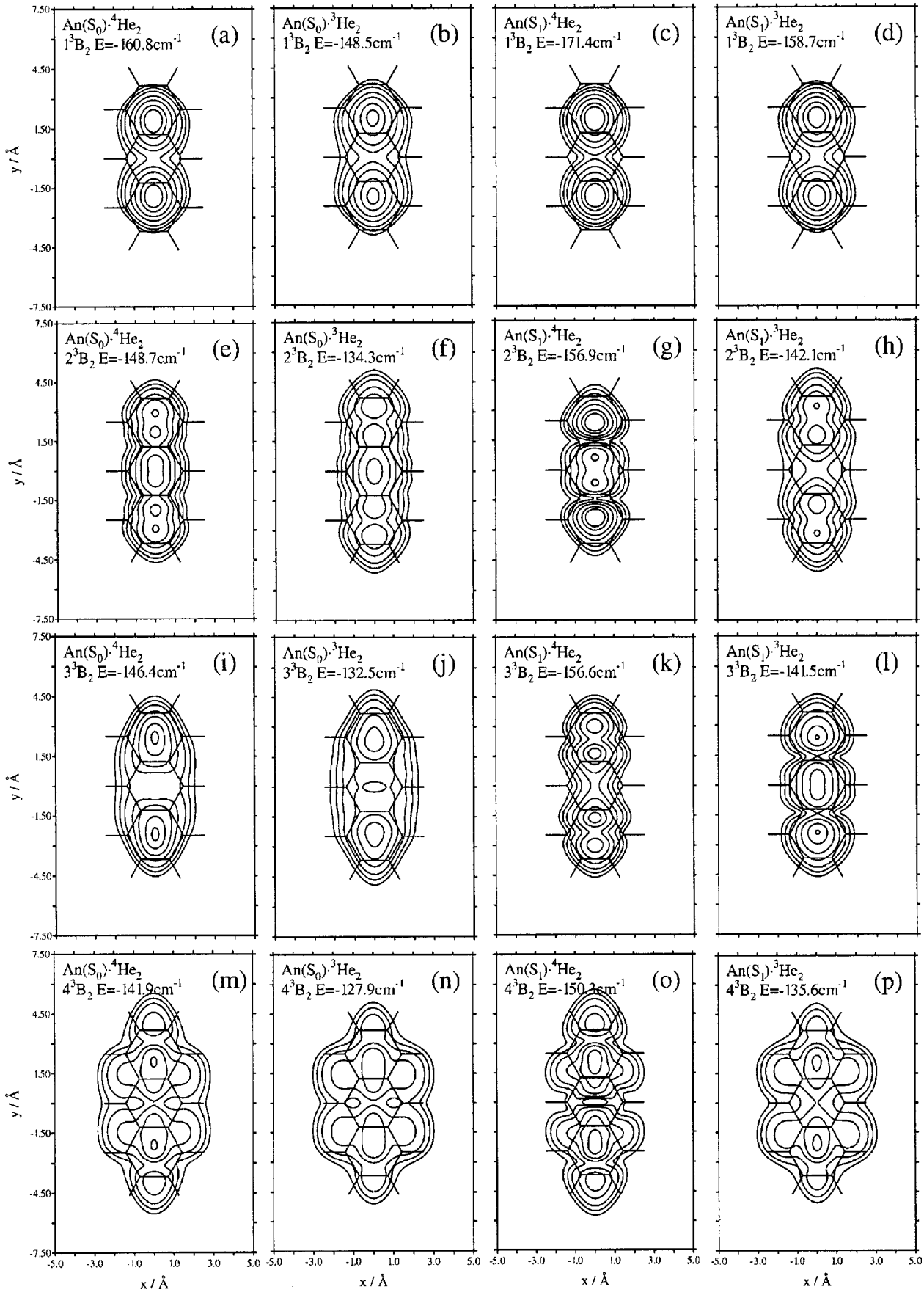

FIG. 14. Contour plots of the one-particle densities of the four lowest $^3B_2$ states of the An·^{4}He$_2$(hyp.) and of the An·^{3}He$_2$ complexes for the S_0 and for the S_1 state anthracene-helium potential. Contour lines are given for density values of 0.005, 0.01, 0.02, 0.05, 0.10, 0.20, and 0.30.

Fig. 12 for the corresponding transitions, is reflected by the spread of the densities. While the 2^1A_1, 2^3B_2, and 3^3B_2 states show the same extension in x direction as their corresponding vibrational ground state wave functions and therefore must be denoted by $[y]$, the 3^1A_1, the 4^1A_1, and the 4^3B_2 state densities are also extended in x direction, indicating their $[xy]$ nature. The shapes of the excited state densities show larger differences, because small perturbations as the change from the S_0 to the S_1 state potential or different masses have a larger influence on the configurational mixing, as the energy separation of the states is smaller.

The spectral shift δ can be approximately estimated by the expectation value of the difference potential $\Delta V = V(S_1) - V(S_0)$, Fig. 1, for the one-particle density $P(x,y,z)$ of the vibrational ground state of S_0,

$$\delta \approx \int_{-\infty}^{\infty} dx \int_{-\infty}^{\infty} dy \int_{-\infty}^{\infty} dz P(x,y,z) \Delta V(x,y,z). \tag{25}$$

Knowing the one-particle density, this approximate expression can provide information concerning parts of the molecule that contribute to the spectral shift. In particular, by comparing the contour plot of the difference potential ΔV, Fig. 1(c), with the one-particle density maps, one can attempt to trace back the origin of the isotope effect $\Delta\delta$ of the spectral shift. For An·He$_1$, $\Delta\delta = 0.28\ \mathrm{cm}^{-1}$, i.e., An·^{3}He$_1$ has a larger ($-1.92\ \mathrm{cm}^{-1}$) red spectral shift than An·^{4}He$_1$ ($-1.62\ \mathrm{cm}^{-1}$) For An·He$_2$ the trend is opposite, $\Delta\delta = -0.50\ \mathrm{cm}^{-1}$, i.e., An·^{4}He$_2$ has a larger red spectral shift ($-10.66\ \mathrm{cm}^{-1}$) than An·^{3}He$_2$ ($-10.16\ \mathrm{cm}^{-1}$). Comparing the density contour maps of the $1A_g$ states of An·He$_1$ [Figs. 5(a) and 5(b)] and of the $1A_1$ states of An·He$_2$ [Figs. 13(a) and 14(b)] with the difference potential [Fig. 1(c)], one sees that a further extension of the one-particle density in the y direction increases the red spectral shift (larger negative contributions), while an extension into x direction causes a blueshift. However, looking at the one-particle densities of the different isotopes of An·He$_1$ and An·He$_2$, it must be stated that the clusters of the lighter helium isotope have a larger spatial extension in both the x and y direction, precluding a simple explanation of the different signs of the isotope differences $\Delta\delta$. The balance of red and blue contributions to the spectral shift is too delicate to explain the different trend in $\Delta\delta$ by simple arguments.

The question arises, how accurate the CI calculations are, i.e., whether basis set A is large enough and whether the treatment of a single-sided C_{2v} framework for the An·He$_2$ system is appropriate. The density of the $18A_g$ state of the An·^{4}He$_1$ complex, Fig. 7(b), provided an indication, how far the density has to reach out into space to cause an appreciable energy splitting. The densities of the An·He$_2$ states depicted in Figs. 13 and 14 are much less extended into space, indicating that splitting due to the interaction of the densities on both sides of the molecular plane is negligible for these states and that the single-sided treatment is justified. However, one may argue that the small basis set A might not be flexible enough to allow for a sufficient spatial expansion of the density, i.e., that the small size of the basis set may conceal possible defects of the one-sided treatment. This raises the question of the convergence of the basis set and of a comparison with experimental data.

In our previous paper[47] we compared the experimental spectra of An·^{4}He$_N$ clusters for $N \leqslant 4$ with the theoretical ones, which were obtained by the one-sided treatment. As guided by the additivity of the spectral redshifts, the An·^{4}He$_2$ complex was treated as two one-sided complexes $(1|0)+(0|1)$, An·^{4}He$_3$ by the complexes $(2|0)+(0|1)$, and the An·^{4}He$_4$ by the two complexes $(2|0)+(0|2)$. That is to say, the calculated spectra of the $(2|0)$ single-sided system have to be compared with the experimental spectra of the clusters $N=3$ and $N=4$. The spectra of the $N=3$ and of the $N=4$ clusters both contain the intense electronic 0-0 origin and only one additional spectral band, which could be unambiguously attributed to the $(2|0)$ system. For both the $N=3$ and the $N=4$ complex, this spectral band is located at 22.5 cm^{-1} relative to the 0-0 band an was assigned by us to the $1^1A_1 \rightarrow 2^1A_1[y]$ transition with the calculated transition energy of 16.5 cm^{-1}.[47] The deviation of 6 cm^{-1} from the experimental value is large compared to the good agreement obtained for the $(1|0)$ complex.[47] The good agreement for the $(1|0)$ complex indicates that the anthracene-helium potential is not the reason for the deviation. Furthermore, the fact that the spectral band was experimentally observed at the same transition energy (22.5 cm^{-1}) for the $N=3$ and for the $N=4$ complex, suggests that the helium atoms on the two different sides of the molecular plane indeed do not communicate. What remains as a likely source of error is the limitation of the 3D basis set.

The diagonal density matrix elements (populations) of the 1D basis functions give insight into the convergence of the CI calculations. The density-matrix elements $P_{\mu x,\nu x}$, $P_{\mu y,\nu y}$, and $P_{\mu z,\nu z}$ are related to the one-dimensional density profiles $P(x)$, $P(y)$, $P(z)$, respectively, cf. Eq. (20):

$$P(x) = N \sum_{\mu x} \sum_{\nu x} P_{\mu x,\nu x} \phi_{\mu x}(x) \phi_{\nu x}(x), \tag{26}$$

where N is the number of particles, i.e., the density profiles $P(x)$, $P(y)$, $P(z)$ are normalized to the number of particles, in this case 2. While the sum of all populations is unity, the individual populations contain the information about the involvement of the corresponding 1D basis functions. Table V contains the populations of the seven lowest A_1 states of the An(S_1)·^{4}He$_2$ system. While the populations $P_{\mu y,\mu y}$ and $P_{\mu z,\mu z}$ are mostly not larger than 0.003 for the highest 1D quantum number, the populations $P_{\mu x,\mu x}$ are larger by one order of magnitude and can reach several percent for $\mu_x = 4$, indicating that the convergence in μ_x is relatively poor. For the S_0 state potential and the two-fermion system, the situation is very similar. Searching for the reason of the large deviation between the theoretical and the experimental energy of the $1^1A_1 \rightarrow 2^1A_1$ transition, Table V indicates that the population for $\mu_x = 4$ is only 0.0012. However, as Table V shows, the populations do not generally decrease monotonously with increasing 1D quantum number. It is therefore imaginable at this stage that the 2^1A_1 state is not really converged. Another possibility is that the 3^1A_1 state, whose population for $\mu_x = 4$ is still 2.4%, repels the 2^1A_1 state and

TABLE V. The populations of the 1D basis functions $\phi_{\mu x}(x)$, $\phi_{\mu y}(y)$, $\phi_{\mu z}(z)$ for the first seven $^1A_1$ states of the An$(S_1)\cdot{}^4He_2$ system.

	$\mu_x=0$	$\mu_x=1$	$\mu_x=2$	$\mu_x=3$	$\mu_x=4$				$\mu_z=0$	$\mu_z=1$	$\mu_z=2$
1^1A_1	0.9880	0.0020	0.0097	0.0000	0.0003				0.9747	0.0227	0.0026
2^1A_1	0.9419	0.0197	0.0366	0.0007	0.0012				0.9689	0.0287	0.0024
3^1A_1	0.5813	0.0646	0.3235	0.0064	0.0242				0.9638	0.0335	0.0026
4^1A_1	0.8643	0.0081	0.1176	0.0006	0.0094				0.9590	0.0385	0.0024
5^1A_1	0.0936	0.8142	0.0599	0.0284	0.0039				0.9552	0.0414	0.0033
6^1A_1	0.4988	0.0251	0.4274	0.0053	0.0434				0.9585	0.0389	0.0026
7^1A_1	0.8224	0.0611	0.1051	0.0037	0.0078				0.9508	0.0462	0.0029
	$\mu_y=0$	$\mu_y=1$	$\mu_y=2$	$\mu_y=3$	$\mu_y=4$	$\mu_y=5$	$\mu_y=6$	$\mu_y=7$	$\mu_y=8$	$\mu_y=9$	$\mu_y=10$
1^1A_1	0.1176	0.3899	0.3710	0.1024	0.0155	0.0015	0.0011	0.0006	0.0001	0.0002	0.0001
2^1A_1	0.1516	0.0610	0.2841	0.3033	0.1594	0.0116	0.0245	0.0015	0.0015	0.0011	0.0004
3^1A_1	0.2326	0.3573	0.2530	0.0419	0.0547	0.0181	0.0356	0.0011	0.0036	0.0015	0.0006
4^1A_1	0.2395	0.1762	0.1475	0.0702	0.1713	0.0788	0.0959	0.0010	0.0159	0.0027	0.0011
5^1A_1	0.1619	0.3782	0.3380	0.0842	0.0251	0.0069	0.0033	0.0008	0.0009	0.0003	0.0002
6^1A_1	0.2949	0.1737	0.2065	0.1540	0.1372	0.0169	0.0131	0.0011	0.0019	0.0004	0.0004
7^1A_1	0.1453	0.2124	0.0984	0.1274	0.0724	0.1198	0.0534	0.0561	0.0809	0.0090	0.0249

lowers its energy by a few wave numbers. This issue will be clarified only by calculations with larger basis sets.

IV. CONCLUDING REMARKS

Our studies of An·He_2 nuclear boson and fermion systems reveal several novel features of the electronic-vibrational level structure of these systems:

(i) Vibrational ground state. While the two-boson An·$^4He_2$ cluster is, of course, in a singlet ground state, the two-fermion An·$^3He_2$ cluster is characterized by a triplet ground state. This result was traced to the dominating He–He two-particle repulsive interactions, which overwhelm the one-particle contributions and result in extensive configuration interaction in the fermion and also in the boson system. The calculated singlet-triplet splitting (1^1B_2-1^3B_2) of 10.7 cm^{-1} in An·$^3He_2$ should be confronted in the future with experiment.

(ii) Vibrational level structure. The tunneling splittings in the An·$^4He_1$ and in the An·$^3He_1$ system becomes apparent (>0.01 cm^{-1}) only for states above a threshold ≈ -22 cm^{-1} (66.9 and 62.2 cm^{-1} above the $1A_g$ ground state of An·$^4He_1$ and An·$^3He_1$, respectively). Since the energy splitting is manifested only for those states whose energy is above the potential-energy barrier of side crossing and whose densities of the helium atoms reach beyond the hydrogen atoms of the aromatic molecule, the energy splitting corresponds to the classical side crossing rather than to tunneling.

(iii) Nuclear dynamics. The communication between two ^4He or two ^3He atoms on two different sides of the anthracene plane goes via the molecular periphery rather than through the molecular plane.

(iv) Isotope effects are rather small. For the zero-point energy of An·$^4He_1$ and An·$^3He_1$ the relative isotope effect is $\approx$12%, in reasonable accord with the mass effect in the harmonic approximation. On the other hand, the relative isotope effect on the difference between the ground states of An·$^4He_2$ and An·$^3He_2$ is 10%, manifesting a partial cancellation of mass and permutation symmetry effects. The isotope effect for the small spectral shift of the electronic origin of the $S_0 \rightarrow S_1$ transition is $\Delta\delta = 0.28$ cm^{-1} for An·He_1. For the An·$^4He_2$ and An·$^3He_2$ clusters the interplay between mass and permutation effects results also in a small value of $\Delta\delta = -0.50$ cm^{-1}, but in the opposite direction.

We implemented the configuration interaction method for the study of two-particle quantum systems, based on symmetry and spin-adapted configurations for boson and fermion systems. The application to the two-boson An·$^4He_2$ system is new, while the treatment of the two-fermion An·$^3He_2$ system, adopted by Jungwirth and Krylov[49] and in the present work is analogous to the traditional approach of many-electron quantum chemistry. The extension of these theoretical approaches to many-particle boson and fermion systems will be of considerable interest in the context of the explanation of nonrigid structures and elementary excitations in these floppy quantum systems.

The theoretical results for the level structure of the An·$^3He_2$ clusters open new horizons for the study of magnetism in the two-fermion (and many-fermion) systems. Our calculations were performed for the $M_S=0$ state, while further studies of the entire $M_S=0,\pm1$ manifold in magnetic fields will be of interest. Even more exciting will be the experimental determination of the singlet-triplet splitting in An·$^3He_2$ from nuclear magnetic-resonance studies, which will be confronted with our predictions.

ACKNOWLEDGMENTS

The authors are indebted to the Inter University Computation Center (IUCC) for granting computation time and for excellent service. The research was supported by the German-Israeli James-Franck program on laser-matter interactions.

[1] *Structure and Dynamics of Clusters*, edited by T. Kondow, K. Kaya, and A. Terasaki (University Press, Tokyo, 1996).
[2] Small Particles and Inorganic Clusters (ISSPIC10 Symposium), Eur. Phys. J. D **16,** 1 2001.
[3] *Small Particles and Inorganic Clusters (ISSP9)*, edited by J. M. Bonard and A. Chatelin (Springer-Verlag, Berlin, 1999).
[4] C. N. R. Rao and A. K. Cheetham, J. Mater. Chem. **11**, 2887 (2001).
[5] J. Jortner and C. N. R. Rao, Nanostructured Advanced Materials, Pure and Applied Chemistry **74**, 1491 (2002).

[6] S. C. Pieper, R. B. Wiringa, and V. R. Pandharipande, Phys. Rev. B **32**, 3341 (1985).
[7] V. R. Pandharipande, S. C. Pieper, and R. B. Wiringa, Phys. Rev. B **34**, 4571 (1986).
[8] M. V. Rama Krishna and K. B. Whaley, J. Chem. Phys. **93**, 6738 (1990).
[9] S. Stringari and J. Treiner, J. Chem. Phys. **87**, 5021 (1987).
[10] D. M. Brink and S. Stringari, Z. Phys. D: At., Mol. Clusters **15**, 257 (1990).
[11] S. A. Chin and E. Krotscheck, Phys. Rev. B **45**, 852 (1992).
[12] M. V. Rama Krishna and K. B. Whaley, Mod. Phys. Lett. B **4**, 895 (1990).
[13] M. Casas, F. Dalfóvo, A. Lastri, L. Serra, and S. Stringari, Z. Phys. D: At., Mol. Clusters **35**, 67 (1995).
[14] M. Casas and S. Stringari, J. Low Temp. Phys. **79**, 135 (1990).
[15] E. Cheng, M. A. McMahon, and K. B. Whaley, J. Chem. Phys. **104**, 2669 (1996).
[16] M. A. McMahon and K. B. Whaley, J. Chem. Phys. **103**, 2561 (1995).
[17] M. A. McMahon, R. N. Barnett, and K. B. Whalley, Z. Phys. B: Condens. Matter **98**, 421 (1995).
[18] P. Sindzingre, M. L. Klein, and C. M. Ceperley, Phys. Rev. Lett. **63**, 1601 (1989).
[19] J. A. Northby, J. Chem. Phys. **115**, 10065 (2001); F. Dalfovo and S. Stringari, *ibid.* **115**, 10078 (2001); D. M. Ceperley and E. Menousakis, *ibid.* **115**, 10111 (2001).
[20] J. P. Toennies and A. F. Vilesov, Annu. Rev. Phys. Chem. **49**, 1 (1998).
[21] M. Hartmann, F. Mielke, J. P. Toennies, A. F. Vilesov, and G. Bedenek, Phys. Rev. Lett. **76**, 4560 (1996).
[22] M. Farnik, U. Henne, B. Samelin, and J. P. Toennies, Phys. Rev. Lett. **81**, 3892 (1998).
[23] S. Grebenev, J. P. Toennies, and A. F. Vilesov, Science **279**, 2083 (1998).
[24] S. Grebenev, N. Portner, A. F. Vilesov, M. Hartmann, A. Lindingers, E. Lugovoi, J. P. Toennies, and E. Sartakov, *Proceedings of the Nobel Symposium*, Vol. 117, The Physics and Chemistry of Clusters (World Scientific, Singapore, 2001), p. 122.
[25] J. Harms, M. Hartmann, B. Sartakov, J. P. Toennies, and A. F. Vilesov, J. Mol. Spectrosc. **185**, 204 (1997).
[26] S. Grebenev, M. Hartmann, M. Havenith, B. Sartakov, J. P. Toennies, and A. F. Vilesov, J. Chem. Phys. **112**, 4485 (2000).
[27] M. Hartmann, R. E. Miller, J. P. Toennies, and A. F. Vilesov, Phys. Rev. Lett. **75**, 1566 (1995).
[28] K. Nauta and R. E. Miller, Phys. Rev. Lett. **82**, 4480 (1999).
[29] C. Callegari, A. Conjusteau, I. Reinhard, K. K. Lehmann, G. Scoles, and F. Dalfovo, Phys. Rev. Lett. **83**, 5058 (1999).
[30] T. Tsuneto, *Superconductivity and Superfluidity* (Cambridge University Press, Cambridge, 1998).
[31] M. Hartmann, A. Lindinger, J. P. Toennies, and A. F. Vilesov, Chem. Phys. **239**, 139 (1998).
[32] R. E. Smalley, L. Wharton, D. H. Levy, and D. W. Chandler, J. Chem. Phys. **68**, 2487 (1978).
[33] S. M. Beck, M. G. Liverman, D. L. Monts, and R. E. Smalley, J. Chem. Phys. **70**, 232 (1979).
[34] D. H. Levy, C. A. Haynam, and D. V. Brumbaugh, Faraday Discuss. **73**, 137 (1982).
[35] T. S. Zwier, E. Carrasquillo, and D. H. Levy, J. Chem. Phys. **78**, 5493 (1983).
[36] C. A. Haynam, D. V. Brumbaugh, and D. H. Levy, J. Chem. Phys. **80**, 2256 (1984).
[37] E. R. Bernstein, K. Law, and M. Schauer, J. Chem. Phys. **80**, 634 (1984).
[38] C. A. Taatjes, W. B. Bosma, and T. S. Zwier, Chem. Phys. Lett. **128**, 127 (1986).
[39] K. Yamanouchi, S. Isogai, and S. Tsuchiya, Chem. Phys. **116**, 123 (1987).
[40] D. O. DeHaan, A. L. Holton, and T. S. Zwier, J. Chem. Phys. **90**, 3952 (1989).
[41] T. S. Zwier, J. Chem. Phys. **90**, 3967 (1989).
[42] D. H. Semmes, J. S. Baskin, and A. H. Zewail, J. Chem. Phys. **92**, 3359 (1990).
[43] B. Coutant and P. Bréchignac, J. Chem. Phys. **100**, 7087 (1994).
[44] A. Bach, S. Leutwyler, D. Sabo, and Z. Bacic, J. Chem. Phys. **107**, 8781 (1997).
[45] U. Even, J. Jortner, D. Noy, N. Lavie, and C. Cossart-Magos, J. Chem. Phys. **112**, 8068 (2000).
[46] I. Al-Hroub, U. Even, and J. Jortner, J. Chem. Phys. **115**, 2069 (2001).
[47] A. Heidenreich, U. Even, and J. Jortner, J. Chem. Phys. **115**, 10175 (2001).
[48] Y. Kwon and K. B. Whaley, J. Chem. Phys. **114**, 3163 (2000).
[49] P. Jungwirth and A. I. Krylov, J. Chem. Phys. **115**, 10214 (2001).
[50] K. F. Lim, J. Chem. Phys. **101**, 8756 (1994).
[51] E. Shalev, N. Ben-Horin, U. Even, and J. Jortner, J. Chem. Phys. **95**, 3147 (1991).
[52] R. J. Vos, J. H. van Lenthe, and F. B. Duijnenveldt, J. Chem. Phys. **93**, 643 (1990).
[53] D. M. Ceperley and H. Partridge, J. Chem. Phys. **84**, 820 (1986).
[54] R. A. Aziz and M. J. Slaman, J. Chem. Phys. **94**, 8047 (1991).